

Class-feature Watermark: A Resilient Black-box Watermark Against Model Extraction Attacks

Yaxin Xiao¹, Qingqing Ye¹, Zi Liang¹, Haoyang Li¹, RongHua Li¹, Huadi Zheng², Haibo Hu^{*1,3}

¹Department of Electrical and Electronic Engineering, The Hong Kong Polytechnic University

²Huawei Technologies Co., Ltd.

³Research Centre for Privacy and Security Technologies in Future Smart Systems

20034165r@connect.polyu.hk, qqing.ye@polyu.edu.hk, {zi1415926.liang, hao-yang9905.li, cory-ronghua.li}@connect.polyu.hk, zhenghuadi@huawei.com, haibo.hu@polyu.edu.hk

Abstract

Machine learning models constitute valuable intellectual property, yet remain vulnerable to model extraction attacks (MEA), where adversaries replicate their functionality through black-box queries. Model watermarking counters MEAs by embedding forensic markers for ownership verification. Current black-box watermarks prioritize MEA survival through representation entanglement, yet inadequately explore resilience against sequential MEAs and removal attacks. Our study reveals that this risk is underestimated because existing removal methods are weakened by entanglement. To address this gap, we propose **Watermark Removal attacK (WRK)**, which circumvents entanglement constraints by exploiting decision boundaries shaped by prevailing sample-level watermark artifacts. WRK effectively reduces watermark success rates by $\geq 88.79\%$ across existing watermarking benchmarks.

For robust protection, we propose **Class-Feature Watermarks (CFW)**, which improve resilience by leveraging class-level artifacts. CFW constructs a synthetic class using out-of-domain samples, eliminating vulnerable decision boundaries between original domain samples and their artifact-modified counterparts (watermark samples). CFW concurrently optimizes both MEA transferability and post-MEA stability. Experiments across multiple domains show that CFW consistently outperforms prior methods in resilience, maintaining a watermark success rate of $\geq 70.15\%$ in extracted models even under the combined MEA and WRK distortion, while preserving the utility of protected models.

Code — <https://github.com/ClassFeatureWatermark/ClassFeatureWatermark>

Introduction

Developing machine learning (ML) models requires substantial investments in data collection, hyper-parameter tuning, and computation resources. To lower these barriers, Machine Learning as a Service (MLaaS) platforms like Google AutoML (Google Cloud 2024), Microsoft Azure ML (Microsoft Azure 2024), and Amazon SageMaker (Amazon Web Services 2017) offer ML inference services for applications like speech recognition (Alharbi et al. 2021) and medical analysis (Chen et al. 2024). However, such models face

the threat of model extraction attacks (MEA) (Tramèr et al. 2016; Liang et al. 2025), where adversaries use black-box queries to replicate model functionality (Zhang et al. 2025). These stolen models can be monetized, which infringes on the intellectual property of model owners and highlights the need for ownership protection.

Black-box model watermarking (Jia et al. 2021) has emerged as a promising forensic solution to protect ownership under MEA. It embeds a watermark task into the protected model. During MEA, the stolen model inherits this task, providing ownership proof. Recent approaches (Jia et al. 2021; Lv et al. 2024) employ backdoor-based watermarks that modify domain inputs with artifacts and assign new labels to create watermark samples. The model’s behavior on these samples serves as the forensic marker. These methods ensure stable transferability in MEA through entanglement with domain tasks in representation spaces.

This focus on MEA survival creates a critical vulnerability: watermarks remain exposed to removal attacks *after* model extraction. Such sequential threats are increasingly practical, as advanced removal techniques (Zhu et al. 2023; Zheng et al. 2022b; Li et al. 2023; Zhang et al. 2024) continue to emerge. If adversaries can strip watermarks post-extraction, ownership verification fundamentally fails, rendering defenses useless precisely when needed most.

This paper investigates watermark resilience against sequential MEA and removal attacks. We expose a critical vulnerability: Existing evaluation underestimates removal attack risks because existing techniques, including trigger inversion (Wang et al. 2019; Aiken et al. 2021), neuron pruning (Liu, Dolan-Gavitt, and Garg 2018; Zheng et al. 2022b), and learning-induced forgetting (Zhu et al. 2023; Li et al. 2021), fail against entangled watermarks. These ill-suited methods compromise resilience assessments, creating a false sense of security.

To provide a more reliable assessment, we propose **Watermark Removal attacK (WRK)**, a removal method that explicitly targets entangled black-box watermarks. WRK reshapes the decision boundary to disrupt regions likely to contain watermarks. Current watermarking paradigms construct watermark samples by injecting artifacts into domain inputs and assigning new labels, which positions the decision boundary between the original and modified samples.

*Corresponding author: haibo.hu@polyu.edu.hk

WRK exploits this geometric vulnerability to disrupt watermark regions. It further incorporates an objective to shift output-layer parameters (Min et al. 2023) to prompt disentanglement. By specifically targeting the backdoor-style constructions, WRK enables more rigorous stress-testing of watermark resilience.

In the second part of this paper, to address the low resilience of backdoor-style watermarks, we introduce **Class-Feature Watermarks (CFW)**. Existing watermarks rely on sample-specific artifacts, which expose watermark regions and make them vulnerable to WRK. CFW addresses this vulnerability with a synthetic watermark class created by labeling diverse out-of-domain (OOD) samples as a unified class. In other words, it maintains essential task distinctiveness at the class level to prevent false ownership claims.

However, deploying a crafted class as a model watermark is insufficient to defend against MEA due to two key challenges. First, the task must exhibit representation entanglement (RE) with domain tasks to ensure transferability during MEA. We address this by introducing a quantitative metric to guide RE during watermark embedding, which also improves resilience by making the watermark less susceptible to learning-induced removal and pruning. Second, to remain resilient in the extracted model, CFW must preserve clustering among its samples in the representation space. Yet, feature variance among CFW samples causes uneven distortion during MEA, which disperses representations. To preserve CFW stability after MEA, we regularize pairwise distances among CFW representations to promote compact clustering.

In summary, this paper makes the following contributions:

- We theoretically establish a positive correlation between watermark transferability in MEA and their resilience to removal attacks, both of which are linked to the underlying property of representation entanglement.
- We identify the overlooked vulnerability of entangled watermarks, and propose **Watermark Removal attackK (WRK)**, which disentangles watermarks from domain tasks by reshaping the associated decision boundaries.
- We propose **Class-Feature Watermarks (CFW)**, a resilient watermarking approach that leverages class-level artifacts to resist WRK. To ensure both effectiveness and resilience during MEA, we optimize its representation entanglement and stability during embedding.
- Comprehensive evaluations show that WRK reduces watermark success rates by $\geq 88.79\%$ across existing black-box benchmarks, whereas eight prior removal methods fail against entangled watermarks. CFW achieves superior resilience, maintaining $\geq 70.15\%$ watermark success rate under combined MEA and WRK attacks across domains while preserving the utility of protected models.

Problem Definition

Machine Learning (ML) Notation. Since model extraction attacks (MEAs) primarily target classifiers (Tramèr et al. 2016; Xiao et al. 2022), we consider a K -class classification model F_θ (abbreviated as F) with parameters θ . F maps inputs $\mathbf{x} \in X \subseteq \mathbb{R}^d$ to discrete labels $y \in Y = \{1, \dots, K\}$. The model comprises L sequential neural network layers,

where layer 1 is the input layer and layer L the output layer. The representation at layer l is denoted $F_{\theta^l}(\mathbf{x})$, with θ^l representing parameters from layers 1 to l . The final layer outputs logits $= F(\mathbf{x}) \in \mathbb{R}^K$. These logits are normalized via softmax to produce class probabilities, with the predicted label given by $\hat{y} = \arg \max_{k \in Y} F(\mathbf{x})_k$.

Model Extraction Attacks (MEAs). In MLaaS, models are deployed as black-box services to protect costly model development and proprietary training data (Microsoft Azure 2024; Google Cloud 2024). Model extraction attacks (MEAs) threaten the intellectual property of these models by stealing functionality through queries (Zheng et al. 2022a).

MEA adversaries replicate victim models F_v into copy models F_s using queried input-output pairs, without accessing internal structures. MEA performance is evaluated by two metrics: 1) **Test accuracy (ACC)** of F_s on the domain test set D_t ; and 2) **Fidelity (FID)** (Zheng et al. 2019; Zhang et al. 2025), which measures the similarity between the victim and copy models by their label agreement rate on D_t . To date, learning-based model extraction is the de-facto approach, where the adversary first queries F_v and then trains F_s using the queried results (Xiao et al. 2022; Pal et al. 2020).

Threat Model. We formalize the threat model as an ownership game between a defender **D**, who owns the victim model F_v and aims to protect its intellectual property, and an adversary **A**, who attempts to steal and misuse the model.

Specifically, the game proceeds as follows: First, **D** embeds a black-box watermark \mathcal{W} into the victim model F_v to later verify ownership. Watermark samples and training data are securely stored on a trusted platform with a timestamp. Then, the adversary **A** steals the model either via model extraction attacks (black-box access) or illegal downloads (white-box access), and obtains a copy model F_s . To evade detection, **A** attempts to remove the watermark from F_s using limited domain data D_d before deploying it as a competing query service. Finally, **D** queries the suspected model F_s using watermark samples to obtain evidence \mathcal{E} regarding the existence of \mathcal{W} . The game outcomes are settled as follows: if the evidence \mathcal{E} confirms the presence of \mathcal{W} in F_s , then **D** wins; otherwise, **A** wins. However, if \mathcal{E} falsely indicates the watermark in an innocent model, **D** loses.

Problem Formulation. To succeed in the ownership game, the model watermarking must meet these criteria: **1 Prop. 1. Utility Preservation.** Watermarks preserve the functionality of the victim model F_v for benign users. **2 Prop. 2. High MEA transferability.** Watermarks persist in F_s across diverse MEA. **3 Prop. 3. Correctness.** The watermark accurately identifies stolen models without false ownership claims. **4 Prop. 4. Removal Resilience.** Watermarks withstand removal attempts. **5 Prop. 5. Stability.** Watermark resilience in F_s consists of that in F_v . **6 Prop. 6. Stealthiness.** Watermarks remain undetectable to adversaries.

Theoretical Analysis of Watermark Resilience

Existing removal methods (Zhu et al. 2023; Zhang et al. 2024) insufficiently evaluate the resilience of black-box watermarks designed for ownership verification in MEA. This is because they overlook representation entanglement (RE)

between watermark and domain tasks (Jia et al. 2021), which is essential for watermark transferability in MEA. We present a theoretical framework showing that RE also underpins resilience against removal attacks, underscoring the need for tailored removal methods to evaluate highly entangled watermarks. Next, we first introduce a metric to quantify RE, then link it to watermark resilience using Neural Tangent Kernel (NTK) theory (Doan et al. 2021).

Quantifying Representation Entanglement (RE)

Representation entanglement (RE) refers to the similarity between representations of watermark and domain tasks. It plays a key role in enabling watermark’s MEA transferability (Jia et al. 2021; Lv et al. 2024), which is evaluated as the watermark success rate in the extracted model. Although RE has been widely acknowledged, a formal definition has been lacking. We address this gap by defining RE as a measurable quantity and linking it to the success of MEA.

Although RE is defined between watermark and domain tasks, it effectively reflects entanglement between watermark and query data that is assumed following the domain distribution. We argue that the minimum cosine similarity across all layers acts as a bottleneck: if the representations of the watermark and query data are orthogonal at any layer, MEA fails.

We illustrate this with a linear model F_θ parameterized by $\theta \in \mathbb{R}^{m \times d}$, trained on dataset $D = X \times Y$, where $X \in \mathbb{R}^{b \times d}$ and $Y \in \mathbb{R}^{b \times m}$. The model satisfies $Y^\top = \theta X^\top$. During MEA, an adversary queries the model with X_q and obtains $Y_q^\top = \theta X_q^\top$. Under this setting, we establish a formal failure condition as follows, and provide its proof in Appendix A (Xiao et al. 2025).

Theorem 1 (MEA Fails with Orthogonal Representations). *Given the linear model above, if all queried outputs are orthogonal to the training outputs, i.e., $\mathbf{y}_q \cdot \mathbf{y}^\top = 0$ for all $\mathbf{y}_q \in Y_q$, $\mathbf{y} \in Y$, then no estimated parameter $\hat{\theta}$ inferred from $X_q \times Y_q$ can satisfy $\hat{\theta} X^\top = \theta X^\top$. In this case, MEA fails to reproduce the model outputs on the original domain.*

Theorem 1 reveals the general failure condition for MEA, which also applies when treating X as watermark data. That is, orthogonal representations between the watermark and query data cause MEA to fail, while higher cosine similarity improves fidelity. Guided by this, we define the RE metric below. Experiments in Appendix B (Xiao et al. 2025) validate its strong correlation with the watermark’s MEA transferability.

Definition 1. (Representation Entanglement (RE) for Black-Box Model Watermarking) *Let F_θ be a neural network with layers $\{L\}$ and feature maps $\psi \in \Psi$, where $\psi : F_{\theta^l}(X) \rightarrow \mathbb{R}^{1 \times m^l}$. Given watermark data $X_w \sim D_w$ and domain data $X \sim D$, the RE is defined as:*

$$\mathcal{RE}(F_\theta; X_w, X) = \inf_{l \in \{L\}, \psi \in \Psi} \left| \frac{\psi(F_{\theta^l}(X_w)) \cdot \psi(F_{\theta^l}(X))^\top}{\|\psi(F_{\theta^l}(X_w))\|_2 \|\psi(F_{\theta^l}(X))\|_2} \right|. \quad (1)$$

Watermark Resilience Correlates with RE

This section establishes the theoretical link between watermark resilience and representation entanglement (RE). Following prior work (Zhang et al. 2024), we categorize removal techniques into three types: (1) trigger reversion (Xu

et al. 2023), (2) learning-induced forgetting (Min et al. 2023), and (3) neuron pruning (Zheng et al. 2022b). Trigger-reversion attacks also rely on learning-induced unlearning to complete the removal process. A watermark is considered resilient only if it withstands all three.

Prior work (Zhang et al. 2024) suggests that the watermark resistance to these removal methods correlates with the NTK cross-kernel norm $\|\phi(X_w)\phi(X)^\top\|_2$, where X_w and X denote the watermark and domain datasets, and $\phi(\cdot) = \nabla_\theta F_\theta(\cdot)$ is the NTK feature map (Doan et al. 2021).

Assuming F_θ is a multi-layer perceptron (MLP), we show in Theorem 2 that this NTK norm is lower bounded by the RE defined in Equation 1.

Theorem 2 (Lower Bound of NTK Cross-Kernel Norm via RE). *Let X_w and X be datasets from the watermark and domain tasks, with sizes N_w and N , respectively. Let F_θ be a neural network, specifically a multi-layer perceptron (MLP). Define $\Gamma = N_w N$. Then the following inequality holds:*

$$\|\phi(X_w)\phi(X)^\top\|_2 \geq \Gamma \cdot \mathcal{RE}(F_\theta; X_w, X). \quad (2)$$

Therefore, RE provides a theoretical foundation for resistance against existing removal methods. The formal proof of Algorithm 2 is given in Appendix A (Xiao et al. 2025).

Watermark Removal Attack (WRK)

Given the limitations of existing removal methods against watermarks designed for ownership verification of MEA-stolen models, we introduce *Watermark Removal attack* (WRK), which explicitly targets highly entangled black-box watermarks (Jia et al. 2021; Lv et al. 2024) to evaluate their true resilience.

High-level Solution. The ideal way to remove entangled watermarks is to unlearn the watermark data from the model (Graves, Nagisetty, and Ganesh 2021). However, this is typically infeasible without access to watermark data, while inversion-based methods (Wang et al. 2019; Xu et al. 2023) largely fail due to the diversity of watermark artifacts. To overcome these limitations, WRK avoids direct inversion and instead perturbs suspicious input regions where watermark tasks are likely to reside. Existing watermarking methods (Jia et al. 2021; Lv et al. 2024) embed artificial patterns into source samples and assign them to target labels. This implies that the decision boundaries lie between the source samples and the corresponding watermark samples. WRK aims to reshape these boundaries to disrupt watermark-related regions.

To implement this idea, WRK follows two key steps. The first, *Boundary Reshaping*, uses large-magnitude adversarial perturbations to generate a set X_p , which targets the broad and variable nature of watermark artifacts. It assigns random labels to X_p to form D_p to enforce stronger boundary shifts between source and perturbed samples. In contrast, adversarial training (AT) (Alexey, Ian, and Samy 2016) applies relatively small perturbations and preserves clean labels, resulting in minimal decision movement. The second step, *Feature Shifting*, resets the final layer and applies a parameter-shift regularization (Min et al. 2023) to further decouple watermark-related features from the primary task.

Algorithm. The adversary **A** has (1) white-box access to the stolen copy model F_s , and (2) a small domain dataset

$D_d \subset X \times Y$ of size N_d . WRK first constructs a perturbing dataset D_p by sampling a subset D'_d of size ρN_d from D_d . For each $\mathbf{x} \in D'_d$, adversarial noise δ_x with magnitude ϵ is computed using FGSM (Alexey, Ian, and Samy 2016). Then, the adversarial sample is formed as $\tilde{x} \leftarrow \text{Clip}(x + \delta_x)$, where the Clip function ensures pixel values are valid. A random label $y \in \{1, \dots, K\}$ is assigned to form the adversarial pair. The resulting set of pairs (\tilde{x}, y) forms D_p . Finally, WRK fine-tunes F_s on $D_{\text{train}} = D_d \cup D_p$ to obtain $F_{s^{\text{wrk}}}$, with a regularization term with coefficient α to encourage the output layer θ^L of F_s shifts from the initial weights θ_{ini}^L . Formally, the fine-tuning loss \mathcal{L}_{wrk} is:

$$\mathcal{L}_{\text{wrk}} = \left[\mathbb{E}_{(x,y) \sim D_{\text{train}}} \mathcal{L}(F_s(x), y) + \alpha \langle \theta^L, \theta_{\text{ini}}^L \rangle \right] \quad (3)$$

The pseudo-code of WRK is provided in Appendix C (Xiao et al. 2025).

Experiments for WRK

We evaluate the resilience of black-box watermarks under WRK, and compare WRK with eight existing removal methods. Ablation studies of WRK and additional results on the Imagenette are provided in Appendix E (Xiao et al. 2025).

Overview of Experimental Setup

We evaluate WRK on four black-box watermarking methods: EWE (Jia et al. 2021), MBW (Kim et al. 2023), MEA-Defender (MEA-D) (Lv et al. 2024), and Blend (Chen et al. 2017). As most methods are designed for image domains, we use CIFAR-10 (Krizhevsky, Hinton et al. 2009) with ResNet18 and ImageNette (Howard 2019) with ResNet50 (see Appendix E.1 (Xiao et al. 2025) for ImageNette results). Two model extraction attacks, MExMI (Xiao et al. 2022) and ActiveThief (Pal et al. 2020), are used with query budgets of 25,000 (CIFAR-10) and 5,000 (ImageNette), respectively. Each removal method can access 5% of the domain samples for CIFAR-10 and 10% for ImageNette. Evaluation metrics include test accuracy (ACC), fidelity (FID), and watermark success rate (WSR). Full details on removal baselines, configurations, MEA settings, WRK hyperparameters, and metric definitions are detailed in Appendix D (Xiao et al. 2025).

Resilience Evaluation of Existing Watermarks

We comprehensively evaluate black-box watermarks from two perspectives: their watermarking effectiveness and their resilience to removal attacks. Table 1 reports the watermark success rate (WSR) on victim models and its transferability to extracted models via MEA. Table 2 shows watermark removal results using WRK and existing removal baselines, with bold indicating the lowest WSR. To assess generality, WRK is also applied to two non-watermark backdoors, WaNet (Nguyen and Tran 2021) and composite (Lin et al. 2020) backdoors, which are excluded from MEA-post watermarking analysis due to their poor transferability.

Watermarking Performance. Table 1 shows that EWE and MEA-Defender achieve strong MEA transferability, while Blend and MBW perform less effectively. Among them, only Blend preserves model accuracy well. In contrast, EWE causes a 1.5% accuracy drop, and both MEA-Defender and MBW incur over 10% degradation, mainly due to MBW’s

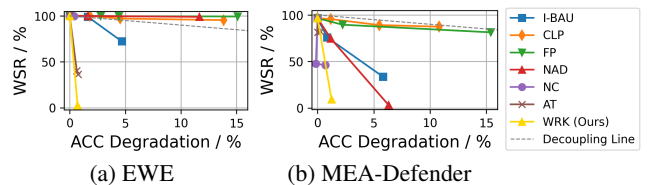


Figure 1: Watermark decoupling curves of victim models. On the decoupling line, ACC and WSR degrade equally.

incompatibility with data augmentation and the complexity of MEA-Defender’s loss design.

Resilience to Removal. Table 2 reports that no existing removal method successfully removes all watermarks and backdoors. EWE, MEA-Defender, and Blend exhibit stronger resilience than MBW, which correlates with their higher representation entanglement (recorded in Appendix B.1). In contrast, WRK consistently reduces all WSRs below non-watermarked baselines while maintaining accuracy within 1.15% of the original model. It also neutralizes all tested backdoors without trigger reversal, which highlights its broad applicability. In the case of MBW, WRK improves accuracy from 73.77% to 82.50% by reintroducing data augmentation during finetuning.

Watermark Decoupling Curves. Figure 1 illustrates the WSR-accuracy trade-off curves for CIFAR-10. Notably, WRK exhibits the steepest curve among the compared methods, achieving a substantial WSR reduction by 91.25% for EWE with only a 0.54% accuracy drop. While FST (Min et al. 2023) performs comparably to WRK on MEA-Defender, it is less effective on EWE. Besides, AT (Alexey, Ian, and Samy 2016) and NC (Wang et al. 2019) fall quickly at first yet stall above 35% WSR, as their reliance on precise trigger/noise inversion limits removal progress.

Class-Feature Watermark (CFW)

Given the vulnerability of existing watermarks to WRK, we focus on designing a resilient black-box watermark that protects against MEA infringement and resists removal attacks.

Class-Level Artifacts for Enhanced Resilience

The weakness of current watermarking schemes under WRK stems from their reliance on sample-level artifacts, where source samples are relabeled to unrelated target classes. This enforced label discrepancy exposes watermarks to removal through decision boundary perturbation.

Therefore, to build a resilient watermark, we avoid sample-level artifacts and instead construct class-level artifacts. This leads to the design of the **Class-Feature Watermark (CFW)**, which maintains task distinctiveness to prevent false ownership claims. Since CFW contains no per-sample patterns, it inherently evades reversion-based methods (Wang et al. 2019). When optimized to enhance its representation entanglement (RE), it further withstands learning-induced forgetting (Li et al. 2021) and neuron pruning (Zheng et al. 2022b).

CFW is formed by assigning samples from multiple out-of-domain (OOD) classes to a single watermark class. It is efficient and task-agnostic, and avoids the cost of high-resolution generation (Zhu et al. 2024). Its class-level ar-

Method	Non-Watermark Model		Victim Model		Copy Model (MEA: MEXMI)			Copy Model (MEA: ActiveThief)		
	ACC	WSR	ACC	WSR	ACC	FID	WSR	ACC	FID	WSR
EWE	93.55±0.19	17.53±2.45	91.98±0.18	99.88±0.12	89.15±0.48	91.52±0.45	99.65±0.35	83.77±0.52	87.16±0.62	99.32±0.68
MBW	93.55±0.19	10.00±0.00	73.77±0.31	100.00±0.0	71.32±1.30	86.99±1.25	10.00±10.0	70.58±0.35	84.99±0.30	10.00±0.00
MEA-D	93.55±0.19	0.96±0.21	85.93±0.10	96.50±0.20	82.15±0.31	84.31±0.28	99.20±0.15	78.08±0.25	81.64±0.22	99.14±0.18
Blend	93.55±0.19	1.53±0.20	93.55±0.08	99.85±0.15	89.97±0.43	91.57±0.12	42.96±0.65	86.88±0.51	89.81±0.48	39.44±12.6

Table 1: Performance of Existing Black-box Watermarks

Removal Metrics	EWE		MBW		MEA-D		Blend		WaNet		Component	
	ACC	WSR	ACC	WSR	ACC	WSR	ACC	WSR	ACC	WSR	ACC	WSR
None	91.98±0.17; 99.88±0.12	73.77±0.31; 100.00±0	85.93±0.25; 96.50±0.20	93.55±0.18; 99.95±0.05	92.19±0.22; 97.69±0.13	92.51±0.23; 94.79±0.35						
NC	N/A	N/A	71.31±0.20; 0.00 ±0.00	86.23±0.15; 47.68±12.7	92.84±0.10; 2.22 ±0.45	N/A; N/A	N/A; N/A	N/A; N/A	N/A; N/A	N/A; N/A	N/A; N/A	N/A; N/A
I-BAU	90.35±0.18; 99.97±0.03	73.15±0.22; 0.00 ±0.00	85.08±0.18; 76.00±12.2	92.15±0.12; 13.24±2.60	91.05±0.15 82.43±5.23	90.61±0.20 90.72±4.20						
BTL-DBF	90.21±0.15; 12.65±2.55	78.82±0.18; 8.00±8.00	84.45±0.12; 32.24±10.2	91.69±0.15; 77.96±4.65	91.97±0.10; 43.19±13.60	93.85±0.48; 90.92±0.30						
CLP	90.17±0.22; 95.60±0.20	76.56±0.30; 60.00±10.0	84.75±0.20; 95.60±0.51	91.62±0.18; 64.24±9.70	90.92±0.20; 51.24±8.65	91.18±0.15; 94.25±0.75						
FP	89.92±0.17; 99.99±0.01	72.50±0.25; 80.00±10.0	83.70±0.22; 89.54±3.23	91.52±0.20; 89.14±0.55	91.58±0.18; 23.12±7.70	91.95±0.12; 94.85±0.20						
NAD	91.80±0.10; 99.98±0.02	71.90±0.15; 10.00±10.0	84.75±0.15; 74.62±11.8	91.56±0.15; 76.43±5.50	91.12±0.15; 70.07±5.45	90.56±0.18; 94.06±0.35						
SEAM	90.49±0.15; 22.89±13.35	81.52±0.10; 0.00 ±0.00	84.05±0.10; 64.62±7.36	91.63±0.10; 87.64±1.45	91.80±0.12; 33.24±6.50	90.55±0.15; 91.45±1.25						
FST	89.96±0.20; 23.55±4.30	83.17±0.12; 6.00±6.00	86.08±0.08; 6.78 ±0.30	92.48±0.08; 57.51±6.75	91.88±0.08; 81.01±5.40	91.07±0.20; 3.80 ±0.50						
WRK	91.44±0.08; 8.75 ±1.75	82.50±0.15; 4.00±6.00	85.46±0.12; 7.64±0.28	92.40±0.07; 9.80±2.35	92.06±0.05; 0.56 ±0.25	91.82±0.15; 6.00±0.30						

Table 2: Performance of WRK and benchmark removal attacks on **victim** models. Results on copy models are provided in Appendix E (Xiao et al. 2025).

tificial distinction arises from the fact that CFW is a non-existent class. To further prevent false claims, CFW ensures that non-watermarked models neither classify these samples as a single category nor cluster their representations. Instead, they should be scattered in the output space. While this scattering occurs naturally, we can further guarantee it by selecting watermark samples using a pre-trained model akin to the step in (Jia et al. 2021). Apart from this diversity constraint in the representation space, CFW introduces an additional safeguard to prevent false positive claims. When the OOD dataset is too distant from the clean task, CFW may yield high false positive rates. To address this, we measure the distance between CFW’s OOD set and the domain set using RBF-MMD, normalized to $[0, 1]$ via $\exp(-\text{distance}^2/\sigma^2)$. CFW claims ownership only when $\text{RBF-MMD} \geq 0.98$.

Overview of CFW. For CFW, its **MEA transferability** guaranteed by representation entanglement (RE) and its **stability** (defined in *Problem Formulation*) in MEA must be achieved. Figure 2 outlines the CFW framework which comprises two primary phases: embedding and verification. In the embedding phase, the model is first trained jointly on the domain and watermark datasets to embed the watermark (Step ①), followed by fine-tuning to enhance RE and stability (Step ②). In the verification phase, CFW uses class-level clustering behavior on the watermark task, which offers more substantial evidence of watermark presence than averaging individual sample predictions.

Optimize RE and Stability of CFW

To enhance representation entanglement (RE) and stability, the fine-tuning phase employs two optimization strategies, both of which are implemented by additional loss terms. Soft Nearest Neighbor Loss (SNNL) is commonly used to increase entanglement by encouraging watermark representations to align with domain features during trigger generation (Jia et al. 2021). However, it is not suitable for our CFW for two reasons. First, CFWs do not include sample-level trigger generation. Second, SNNL jointly optimizes the

model and temperature parameters, making it challenging to strike a balance between RE and model utility. To overcome these issues, we design a **Representation Similarity (RepS)** loss that directly maximizes the cosine similarity between the average representations of watermark and domain data across layers, as guided by the metric \mathcal{RE} . For watermark data $X_w \sim D_w$ and domain data $X \sim D$, the RepS loss is defined as:

$$\mathcal{L}_{\text{RepS}} = \sum_{l=l_0}^L \left| \frac{\psi(F_{\theta l}(X_w)) \cdot \psi(F_{\theta l}(X))^\top}{\|\psi(F_{\theta l}(X_w))\|_2 \|\psi(F_{\theta l}(X))\|_2} \right|, \quad (4)$$

where l_0 is a selected intermediate layer and $\psi : F_{\theta l}(X) \rightarrow \mathbf{R}^{1 \times m^l}$ computes the mean vectors of representations.

In addition to RE, another crucial factor for watermark robustness is the stability of watermark representations under MEA. To this end, we introduce the **Change of Distance under Distortion** loss, denoted as $\mathcal{L}_{\text{CD}^2}$, which aims to preserve intra-class clustering of watermark samples during MEA. Starting from the approximated copy model \hat{F} extracted by MEA, we define the original objective as:

$$\mathcal{L}_{\text{CD}^2} = \frac{1}{N_w^2} \sum_{\mathbf{x}_i, \mathbf{x}_j \in X_w} |\hat{F}(\mathbf{x}_i) - \hat{F}(\mathbf{x}_j)|. \quad (5)$$

To make this formulation tractable, we approximate \hat{F} using neural tangent kernel (NTK) theory (Bennani, Doan, and Sugiyama 2020). As such, the close-form CD^2 loss is theoretically derived from Equation 5 as follows:

$$\mathcal{L}_{\text{CD}^2} = \frac{1}{N_w^2} \sum_{\mathbf{x}_i, \mathbf{x}_j \in D_w} |(F_{\theta L-1}(\mathbf{x}_j) - F_{\theta L-1}(\mathbf{x}_i)) V_{\theta L}|, \quad (6)$$

where $V_{\theta L}$ denotes the right singular vectors of the domain representation matrix, *i.e.*, $V_{\theta L} = \text{SVD}(F_{\theta L-1}(X))$. Complete derivation is in Appendix A (Xiao et al. 2025). Intuitively, $V_{\theta L}$ captures the dominant distortion directions introduced by MEA in the representation space. Appendix B (Xiao et al. 2025) empirically supports this by showing that MEA-induced updates align with the principal components found in $V_{\theta L}$. Since the theory is derived for binary classification, we compute $V_{\theta L}$ separately for each domain class in practice. Combining the above, our final fine-tuning objective becomes:

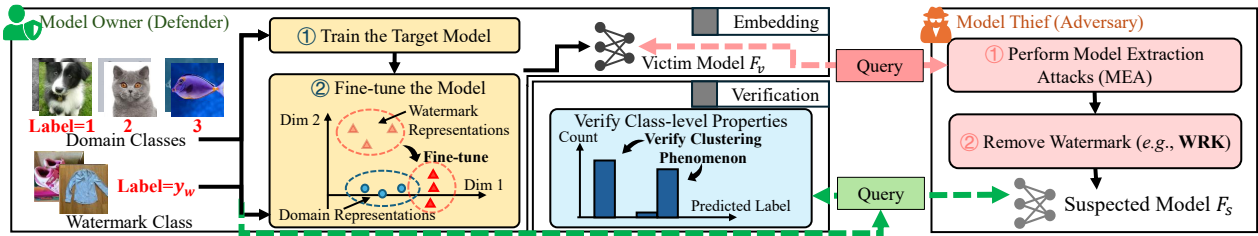


Figure 2: Overall framework of Class-Feature Watermark (CFW).

$$\mathcal{L} = \mathcal{L}_{\text{Cri}} - \lambda_1 \mathcal{L}_{\text{RepS}} + \lambda_2 \mathcal{L}_{\text{CD}^2}, \quad (7)$$

where \mathcal{L}_{Cri} is the criterion loss that preserves both domain utility and watermark accuracy:

$$\mathcal{L}_{\text{Cri}} = \frac{1}{N} \sum_{\mathbf{x} \in \mathcal{X}} \mathcal{L}(F(\mathbf{x}), F_1(\mathbf{x})) + \frac{1}{N_w} \sum_{(\mathbf{x}, y) \in D_w} \mathcal{L}(F(\mathbf{x}), y), \quad (8)$$

and $\lambda_1, \lambda_2 > 0$ are weighting factors for the auxiliary terms. The computation of \mathcal{L} incurs complexity of $O(B_w^2 DK)$, where B_w is the batch size of watermark samples and D is the dimension of the L -layer output. This complexity is minimal and incurs negligible overhead, as B_w is typically much smaller than the domain batch size.

Resilience Bonus of CD^2 Optimization. Beyond improving post-MEA resilience, CD^2 optimization also enhances robustness against learning-induced removal, because the removal-post model \hat{F} shares the same NTK-form approximation with the MEA-post model. As a result, minimizing $\mathcal{L}_{\text{CD}^2}$ preserves intra-class cohesion not only during extraction but also in the learning-induced removal process.

Verify CFW with Intra-class Clustering

Watermark verification is a hypothesis test with two possible outcomes: Hypothesis 0 (H_0) assumes the model is watermarked, while Hypothesis 1 (H_1) asserts it is not. Existing methods (Jia et al. 2021; Lv et al. 2024) typically apply t-tests and use the watermark success rate (WSR) as the test statistic (Jia et al. 2021). However, these approaches ignore the class-level structure in CFWs. Given their enhanced stability, our verification method prioritizes group clustering (Jin et al. 2023) over individual predictions. Next, we explore why clustering provides a more resilient verification evidence than prediction accuracy (*i.e.*, watermark success rate, WSR).

Clustering is a Resilient Evidence for Watermark Presence. To compare the resilience of intra-class clustering and WSR, we apply the WRK attack to class-feature watermarks. This attack perturbs the sample-wise artifacts and leverages learning-induced forgetting, making it a strong testbed for resilience.

Experiments. Experiments are conducted on CIFAR-10 with ResNet-18, using 250 out-of-domain (OOD) samples from CIFAR-20 to create the watermark task, whose clustering is optimized with CD^2 . In this setting, CFW shows a weak correlation between WSR and clustering, making it ideal for our comparison. Figure 3 uses t-SNE (Van der Maaten and Hinton 2008) to visualize the final-layer representations and WSR (see Equation 31) for three models: the original watermarked model, the WRK-attacked watermarked model, and a non-watermarked model. Figure 3b

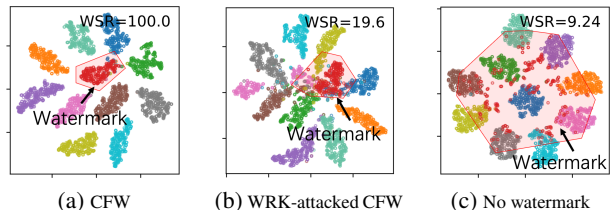


Figure 3: Visualized representations of the last hidden layer.

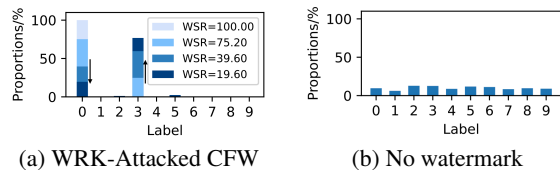


Figure 4: Predicted label histograms during WRK attacks.

shows that despite WSR dropping from 100% to 19.6%, representations remain well-clustered, indicating clustering is more resilient than WSR.

Verify with Clustering in Label-only Access. Since clustering is more resilient than WSR, we propose to verify CFW by checking for clustering. However, in practice, the verifier may only have **label-only** access. In this case, we observe whether label distributions imply clustering in the watermark class. Thanks to the stability enforced by CD^2 optimization, we infer that its logits are still highly consistent during removal. As a result, label distributions may reveal clustering patterns even when WSR suggests failure. This phenomenon is referred to as label clustering.

Label Clustering. We define a *deformation label* to describe new cluster centers that emerge after removal. Figure 4a shows label histograms of the watermark task during WRK attacks performed in the section titled *Experiments for WRK*. After removal, strong clustering persists on both the watermark label (= 0) and a deformation label (= 3), due to intra-class representation clustering. Thus, verification with clustering is conducted to evaluate whether the watermark and deformation labels exhibit clustering. The deformation label is not always identical but is predictable and related to the watermark label rather than the watermark samples, which are discussed in Appendix B (Xiao et al. 2025).

Experiments for Class-feature Watermarks

Overview of Experimental Setup

We evaluate five tasks spanning three domains: ResNet-18 (He et al. 2016) trained on **image** datasets (CIFAR-

Non-watermark		Victim Model				Copy Model						
No Removal		No Removal		WRK Removal		MEA	No Removal			WRK Removal		
ACC	WSR _{LC}	ACC	WSR _{LC}	ACC	WSR _{LC}		ACC	FID	WSR _{LC}	ACC	FID	WSR _{LC}
CIFAR-10												
93.55±0.19;12.00±2.67		93.26±0.12;100.00±0		91.95±0.12;96.67±0.67		MEaMI	89.29±1.12;92.70±1.06;94.00±1.33	88.94±0.95;90.13±1.12; 79.33±2.67				
						ActiveThief	85.89±1.18;88.34±1.18;88.00±0.67	87.26±1.21;89.27±1.24; 74.67±2.00				
CIFAR-20												
81.61±0.35;6.67±0.67		81.26±0.32;100.00±0		80.54±0.21;96.67±0.67		MEaMI	80.64±1.24;82.35±1.36;85.33±1.33	80.18±1.27;81.97±1.42; 70.67±2.67				
						ActiveThief	71.41±1.33;77.47±1.48;81.33±1.92	72.15±1.36;77.30±1.54; 64.67±1.33				
Imagenette												
88.12±0.28;11.35±0.71		85.42±0.55;100.00±0		84.35±0.42;95.33±3.56		MEaMI	86.04±1.39;83.92±0.66;86.67±2.00	84.35±0.92;82.93±0.72; 76.67±1.23				
						ActiveThief	85.32±1.14;82.51±0.78;83.33±1.33	84.49±0.88;81.92±0.84; 73.33±1.33				
DBPedia												
98.17±0.09;15.39±0.75		98.03±0.09;100.00±0		97.85±0.21;94.92±0.45		MEaMI	95.15±0.71;96.62±0.96;97.33±0.38	94.83±0.54;95.76±1.02; 88.72±0.42				
						ActiveThief	91.35±0.87;92.82±1.08;94.32±0.57	91.51±0.63;93.05±1.14; 80.64±0.61				
Speech Commands												
97.36±0.12;8.66±0.47		97.02±0.14;100.00±0		96.03±0.24;95.33±0.27		MEaMI	96.46±0.66;97.82±1.26;95.00±0.73	95.96±0.69;96.79±1.32; 82.12±0.87				
						ActiveThief	96.33±0.72;97.73±1.38;94.00±0.99	94.61±0.75;95.20±1.44; 79.35±1.11				

Table 3: Performance of Class-feature Watermark (CFW) Against WRK Removal

Watermarks	Victim Model						Copy Model					
	Metrics	$\mathcal{RE}\uparrow$	$CD^2\downarrow$	ACC	WSR	WSR _{LC}	Var($\times 10^2$)	ACC	FID	WSR	WSR _{LC}	Var($\times 10^2$)
w/o CD^2 , RepS	0.19±0.06	3.98±0.25	93.70±0.15	100.00±0.0	100.00±0.0	2.59±0.44	89.55±1.23	92.54±1.13	57.33±2.00	70.00±2.67	10.30±3.25	
w/ SNNL only	0.85±0.05	2.51±0.18	90.13±0.22	99.33±0.15	100.00±0.0	4.14±1.21	87.18±1.14	90.49±0.97	73.33±2.00	77.33±2.67	11.12±3.78	
w/ RepS only	0.92±0.04	1.78±0.15	93.31±0.12	100.00±0.0	100.00±0.0	1.92±0.64	89.85±1.18	92.85±1.28	92.00±1.33	94.00±1.33	8.17±2.84	
w/ CD^2 only	0.04±0.03	0.059±0.008	93.40±0.14	100.00±0.0	100.00±0.0	1.35±1.02	89.85±1.21	92.11±1.32	68.67±2.00	84.00±2.67	2.47±1.01	
CFW	0.75±0.06	0.081±0.010	93.26±0.12	100.00±0.0	100.00±0.0	1.68±0.52	89.29±1.12	92.70±1.06	91.33±1.33	94.00±1.33	2.74±0.90	

Arrows represent the trend toward better watermark performance.

Table 4: Evaluation Results of Class-feature Watermark (CFW) Variants

10, CIFAR-20 (Krizhevsky, Hinton et al. 2009)), ResNet-50 (He et al. 2016) trained on ImageNette (Howard 2019), DPCNN (Johnson and Zhang 2017) with BERT embeddings trained on a **text** dataset (DBPedia (Auer et al. 2007)), and VGG19-BN (Simonyan and Zisserman 2014) trained on an **audio** dataset (Speech Commands (Warden 2018)). The CFW dataset is built using multi-class OOD samples assigned to a single label, with size constrained to 0.2%–0.3% of the domain dataset. The watermark samples and MEA query pool are strictly disjoint, with no overlap in classes or distributions. For clustering-based verification, we introduce two metrics: intra-class variance (Var) measuring representation compactness, and label clustering (WSR_{LC}), defined as the sum of WSRs over watermark and deformation labels. Detailed CFW settings, MEA setups, and metric definitions are provided in Appendix D (Xiao et al. 2025).

Overall Evaluation of CFW

We evaluate Class-Feature Watermarks (CFW) against the six properties defined in the ownership game. Table 3 summarizes performance under WRK, focusing on utility preservation (**Prop.1**), MEA transferability (**Prop.2**), correctness (**Prop.3**), and resilience on both victim and copy models (**Prop.4, Prop.5**). Besides, Appendix E (Xiao et al. 2025) further evaluates: (1) resilience comparison between CFW and baseline watermarks using WSR and WSR_{LC} metrics, (2) resilience under additional removal attacks, (3) impacts of CD^2 and RepS optimization, (4) generalization across architectures, and (5) stealthiness (**Prop.6**) through anomaly detection analysis.

Results. CFW achieves near-perfect label clustering rates (WSR_{LC} = 100%) on watermarked victim models, enabling high-confidence verification. The watermark trans-

fers consistently to copy models extracted via MEA, with WSR_{LC} exceeding 81.33% before removal, which attributes to the RepS optimization. Additionally, model utility degradation remains bounded at $\leq 0.4\%$ except for ImageNette, outperforming existing black-box watermarks which cause $> 1.5\%$ degradation (Table 1). On ImageNette, CFW leads to a 2% utility drop because high-resolution inputs amplify the impact of OOD entanglement on the domain task, but its utility remains comparable to benchmarks. Lastly, CFW demonstrates exceptional resilience against removal attacks. Victim models maintain WSR_{LC} $\geq 94.67\%$ under WRK attacks, while copy models preserve WSR_{LC} $\geq 70.15\%$ despite the combined distortion of MEA and WRK. This robustness stems from two factors: CFW resists WRK’s *Boundary Reshaping* by removing vulnerable decision boundaries, and withstands WRK’s *Feature Shifting* with clustering-based verification, since *Feature Shifting* has a trivial effect on disrupting the representation clustering.

Evaluation on CFW Variants

We ablate the two CFW optimization components: RepS and CD^2 , and compare RepS with the SNNL (Kornblith et al. 2019) algorithm for representation entanglement. The experiments are conducted on CIFAR-10 and further evaluate representation entanglement (\mathcal{RE} , Equation 1) and pairwise distance projections on distortion (CD^2 , Equation 6) metrics. Table 4 presents quantitative results and Figure 5 shows watermark decoupling curves.

Results. RepS and SNNL both enhance \mathcal{RE} (0.92 and 0.85 vs. baseline 0.19), but SNNL degrades accuracy by $> 3\%$ while delivering inferior transferability. In contrast, RepS maintains model utility ($\Delta ACC < 0.4\%$) while achieving higher \mathcal{RE} and copy WSR_{LC} (94.00% vs. SNNL’s 77.33%).

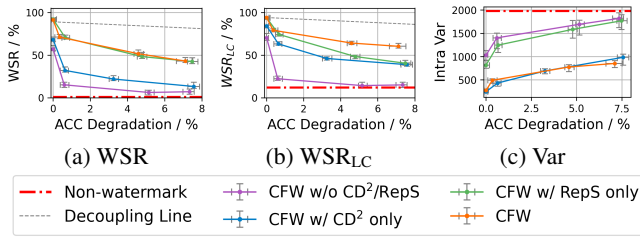


Figure 5: Watermark decoupling curves for CFW on extracted copy models. Vertical lines show the error bars. Appendix E.3 presents corresponding curves on victim models.

Then, CD^2 optimization reduces CD^2 loss by $30\times$ (to 8.10×10^{-2}) and constrains copy model variance to 2.74×10^2 , which is comparable to victim models (1.68×10^2) and $3.8\times$ lower than the baseline. This directly enhances WSR_{LC} from 70.00% to 94.00% in the full CFW implementation. Finally, Figure 5 demonstrates that WSR_{LC} consistently provides clearer evidence than WSR. While RepS only improves WSR resilience, it fails to maintain intra variance clustering. CD^2 optimization enables both robust clustering stability and attack resilience, with CD^2 only variants maintaining label and representation clustering even when WSR drops below 20%.

Related Works

Black-box Watermarks and Their Resilience to Removal. Model watermarking is a promising technique for verifying ownership of machine learning models. While early work showed MEAs could strip watermarks (Lukas et al. 2022), recent breakthroughs demonstrate that black-box watermarks can survive extraction attacks by leveraging representation entanglement (RE) (Jia et al. 2021; Lv et al. 2024). However, their resilience against consecutive MEA and watermark removal attacks remains unevaluated.

Existing removal methods exploit three decoupling strategies: **reversion-based removal**, which reconstructs and erases watermark triggers (NC (Wang et al. 2019), I-BAU (Zeng et al. 2022), DTI-DBF (Xu et al. 2023), Aiken (Aiken et al. 2021)); **neuron pruning**, which eliminates neurons associated with watermark tasks (FP (Liu, Dolan-Gavitt, and Garg 2018), CLP (Zheng et al. 2022b)); and **learning-induced forgetting**, which removes non-domain features via fine-tuning (NAD (Li et al. 2021), SEAM (Zhu et al. 2023), FST (Min et al. 2023)). Watermarks with weak entanglement, such as RS (Bansal et al. 2022) and MBW (Lukas et al. 2022), are vulnerable to all three strategies. Strongly entangled watermarks like EWE (Jia et al. 2021) and MEA-D (Lv et al. 2024) resist most removal attacks but remain vulnerable to DTI-DBF and FST. On the other hand, the two removal methods show limited effectiveness against entangled Blend-type watermarks.

Conclusion

This paper first exposes resilience gaps in black-box watermarks against model extraction attacks (MEA). While existing removal methods are often constrained by the representation entanglement deliberately designed in these watermarks, our Watermark Removal attack (WRK) overcomes

this entanglement barrier by exploiting decision boundaries shaped by their sample-level artifacts. To address the vulnerability exposed by WRK, we introduce Class-Feature Watermarks (CFWs) which shift to class-level artifacts for enhanced resilience and further optimize representation entanglement and stability during MEA. CFW achieves watermark success rates of $\geq 70.15\%$ under combined MEA and WRK attacks across domains, significantly outperforming prior methods in resilience.

Acknowledgments

This work was supported by the National Natural Science Foundation of China (Grant No: 92270123), and the Research Grants Council (Grant No: 15209922, 15210023, 15224124 and 15207725), Hong Kong SAR, China.

References

- Aiken, W.; Kim, H.; Woo, S.; and Ryoo, J. 2021. Neural network laundering: Removing black-box backdoor watermarks from deep neural networks. *Computers & Security*, 106: 102277.
- Alexey, K.; Ian, G.; and Samy, B. 2016. Adversarial machine learning at scale. *arXiv preprint arXiv:1611.01236*.
- Alharbi, S.; Alrazgan, M.; Alrashed, A.; Alnomasi, T.; Almojel, R.; Alharbi, R.; Alharbi, S.; Alturki, S.; Alshehri, F.; and Almojil, M. 2021. Automatic speech recognition: Systematic literature review. *Ieee Access*, 9: 131858–131876.
- Amazon Web Services. 2017. Amazon SageMaker. <https://aws.amazon.com/sagemaker/>, Accessed: 2024-12-22.
- Auer, S.; Bizer, C.; Kobilarov, G.; Lehmann, J.; Cyganiak, R.; and Ives, Z. 2007. Dbpedia: A nucleus for a web of open data. In *international semantic web conference*, 722–735. Springer.
- Bansal, A.; Chiang, P.-y.; Curry, M. J.; Jain, R.; Wington, C.; Manjunatha, V.; Dickerson, J. P.; and Goldstein, T. 2022. Certified neural network watermarks with randomized smoothing. In *International Conference on Machine Learning*, 1450–1465. PMLR.
- Bennani, M. A.; Doan, T.; and Sugiyama, M. 2020. Generalisation guarantees for continual learning with orthogonal gradient descent. *arXiv preprint arXiv:2006.11942*.
- Bottou, L. 2010. Large-scale machine learning with stochastic gradient descent. In *Proceedings of COMPSTAT*, 177–186. Springer.
- Breunig, M. M.; Kriegel, H.-P.; Ng, R. T.; and Sander, J. 2000. LOF: Identifying density-based local outliers. In *Proceedings of the 2000 ACM SIGMOD International Conference on Management of Data*, 93–104. ACM.
- Chen, R.; Duffy, Á.; Petrazzini, B. O.; Vy, H. M.; Stein, D.; Mort, M.; Park, J. K.; Schlessinger, A.; Itan, Y.; Cooper, D. N.; et al. 2024. Expanding drug targets for 112 chronic diseases using a machine learning-assisted genetic priority score. *Nature Communications*, 15(1): 8891.
- Chen, X.; Liu, C.; Li, B.; Lu, K.; and Song, D. 2017. Targeted backdoor attacks on deep learning systems using data poisoning. *arXiv preprint arXiv:1712.05526*.

- Deng, J.; Dong, W.; Socher, R.; Li, L.-J.; Li, K.; and Fei-Fei, L. 2009. Imagenet: A large-scale hierarchical image database. In *2009 IEEE conference on computer vision and pattern recognition*, 248–255. Ieee.
- Doan, T.; Bennani, M. A.; Mazouze, B.; Rabusseau, G.; and Alquier, P. 2021. A Theoretical Analysis of Catastrophic Forgetting through the NTK Overlap Matrix. In Banerjee, A.; and Fukumizu, K., eds., *The 24th International Conference on Artificial Intelligence and Statistics, AISTATS 2021, April 13-15, 2021, Virtual Event*, volume 130 of *Proceedings of Machine Learning Research*, 1072–1080. PMLR.
- Google Cloud. 2024. Google AutoML. <https://cloud.google.com/automl>, Accessed: 2024-12-22.
- Graves, L.; Nagisetty, V.; and Ganesh, V. 2021. Amnesiac machine learning. In *Proceedings of the AAAI Conference on Artificial Intelligence*, volume 35, 11516–11524.
- Gu, T.; Liu, K.; Dolan-Gavitt, B.; and Garg, S. 2019. Badnets: Evaluating backdooring attacks on deep neural networks. *IEEE Access*, 7.
- He, K.; Zhang, X.; Ren, S.; and Sun, J. 2016. Deep residual learning for image recognition. In *Proceedings of the IEEE conference on computer vision and pattern recognition*, 770–778.
- Howard, J. 2019. Imagenette. <https://github.com/fastai/imagenette>, Accessed: 2025-04-19.
- Jia, H.; Choquette-Choo, C. A.; Chandrasekaran, V.; and Papernot, N. 2021. Entangled watermarks as a defense against model extraction. In *30th USENIX security symposium (USENIX Security 21)*, 1937–1954.
- Jin, Y.; Zhang, X.; Lou, J.; Ma, X.; Wang, Z.; and Chen, X. 2023. Explaining adversarial robustness of neural networks from clustering effect perspective. In *Proceedings of the IEEE/CVF International Conference on Computer Vision*, 4522–4531.
- Johnson, R.; and Zhang, T. 2017. Deep pyramid convolutional neural networks for text categorization. In *Proceedings of the 55th Annual Meeting of the Association for Computational Linguistics (Volume 1: Long Papers)*, 562–570.
- Kim, B.; Lee, S.; Lee, S.; Son, S.; and Hwang, S. J. 2023. Margin-based neural network watermarking. In *International Conference on Machine Learning*, 16696–16711. PMLR.
- Kornblith, S.; Norouzi, M.; Lee, H.; and Hinton, G. 2019. Similarity of neural network representations revisited. In *International conference on machine learning*, 3519–3529. PMLR.
- Krizhevsky, A.; Hinton, G.; et al. 2009. Learning multiple layers of features from tiny images.
- Li, Y.; Lyu, X.; Koren, N.; Lyu, L.; Li, B.; and Ma, X. 2021. Neural Attention Distillation: Erasing Backdoor Triggers from Deep Neural Networks. In *9th International Conference on Learning Representations, ICLR 2021, Virtual Event, Austria, May 3-7, 2021*. OpenReview.net.
- Li, Y.; Lyu, X.; Ma, X.; Koren, N.; Lyu, L.; Li, B.; and Jiang, Y.-G. 2023. Reconstructive neuron pruning for backdoor defense. In *International Conference on Machine Learning*, 19837–19854. PMLR.
- Liang, Z.; Ye, Q.; Wang, Y.; Zhang, S.; Xiao, Y.; Li, R.; Xu, J.; and Hu, H. 2025. "Yes, My LoRD." Guiding Language Model Extraction with Locality Reinforced Distillation. In *Proceedings of the 63rd Annual Meeting of the Association for Computational Linguistics (Volume 1: Long Papers), ACL 2025, Vienna, Austria*. Association for Computational Linguistics.
- Lin, J.; Xu, L.; Liu, Y.; and Zhang, X. 2020. Composite backdoor attack for deep neural network by mixing existing benign features. In *Proceedings of the 2020 ACM SIGSAC Conference on Computer and Communications Security*, 113–131.
- Liu, F. T.; Ting, K. M.; and Zhou, Z.-H. 2008. Isolation Forest. In *2008 Eighth IEEE International Conference on Data Mining*, 413–422. IEEE.
- Liu, J.; Zhang, R.; Szyller, S.; Ren, K.; and Asokan, N. 2024. False claims against model ownership resolution. In *33rd USENIX Security Symposium (USENIX Security 24)*, 6885–6902.
- Liu, K.; Dolan-Gavitt, B.; and Garg, S. 2018. Fine-pruning: Defending against backdooring attacks on deep neural networks. In *International symposium on research in attacks, intrusions, and defenses*, 273–294. Springer.
- Lukas, N.; Jiang, E.; Li, X.; and Kerschbaum, F. 2022. SoK: How Robust is Image Classification Deep Neural Network Watermarking? In *43rd IEEE Symposium on Security and Privacy, SP 2022, San Francisco, CA, USA, May 22-26, 2022*, 787–804. IEEE.
- Lv, P.; Ma, H.; Chen, K.; Zhou, J.; Zhang, S.; Liang, R.; Zhu, S.; Li, P.; and Zhang, Y. 2024. MEA-Defender: A Robust Watermark against Model Extraction Attack. *2024 IEEE Symposium on Security and Privacy (SP)*.
- Microsoft Azure. 2024. Azure Machine Learning by Microsoft. <https://azure.microsoft.com/en-us/products/machine-learning/>, Accessed: 2024-12-22.
- Min, R.; Qin, Z.; Shen, L.; and Cheng, M. 2023. Towards stable backdoor purification through feature shift tuning. *Advances in Neural Information Processing Systems*, 36: 75286–75306.
- Nguyen, T. A.; and Tran, A. T. 2021. WaNet - Imperceptible Warping-based Backdoor Attack. In *9th International Conference on Learning Representations, ICLR 2021, Virtual Event, Austria, May 3-7, 2021*. OpenReview.net.
- Pal, S.; Gupta, Y.; Shukla, A.; Kanade, A.; Shevade, S.; and Ganapathy, V. 2020. Activethief: Model extraction using active learning and unannotated public data. In *Proceedings of the AAAI Conference on Artificial Intelligence*, 865–872.
- Sandler, M.; Howard, A.; Zhu, M.; Zhmoginov, A.; and Chen, L.-C. 2018. Mobilenetv2: Inverted residuals and linear bottlenecks. In *Proceedings of the IEEE conference on computer vision and pattern recognition*, 4510–4520.
- Simonyan, K.; and Zisserman, A. 2014. Very deep convolutional networks for large-scale image recognition. *arXiv preprint arXiv:1409.1556*.

- Tramèr, F.; Zhang, F.; Juels, A.; Reiter, M. K.; and Ristenpart, T. 2016. Stealing machine learning models via prediction {APIs}. In *25th USENIX security symposium (USENIX Security 16)*, 601–618.
- Van der Maaten, L.; and Hinton, G. 2008. Visualizing data using t-SNE. *Journal of machine learning research*, 9(11).
- Wang, B.; Yao, Y.; Shan, S.; Li, H.; Viswanath, B.; Zheng, H.; and Zhao, B. Y. 2019. Neural cleanse: Identifying and mitigating backdoor attacks in neural networks. In *2019 IEEE symposium on security and privacy (SP)*, 707–723. IEEE.
- Warden, P. 2018. Speech commands: A dataset for limited-vocabulary speech recognition. *arXiv preprint arXiv:1804.03209*.
- Xiao, Y.; Ye, Q.; Hu, H.; Zheng, H.; Fang, C.; and Shi, J. 2022. MExMI: Pool-based active model extraction crossover membership inference. *Advances in Neural Information Processing Systems*, 35: 10203–10216.
- Xiao, Y.; Ye, Q.; Liang, Z.; Li, H.; Li, R.; Zheng, H.; and Hu, H. 2025. Class-feature Watermark: A Resilient Black-box Watermark Against Model Extraction Attacks. *arXiv preprint arXiv:2511.07947*.
- Xu, X.; Huang, K.; Li, Y.; Qin, Z.; and Ren, K. 2023. Towards reliable and efficient backdoor trigger inversion via decoupling benign features. In *The Twelfth International Conference on Learning Representations*.
- Zeng, Y.; Chen, S.; Park, W.; Mao, Z.; Jin, M.; and Jia, R. 2022. Adversarial Unlearning of Backdoors via Implicit Hypergradient. In *The Tenth International Conference on Learning Representations, ICLR 2022, Virtual Event, April 25-29, 2022*. OpenReview.net.
- Zhang, K.; Cheng, S.; Shen, G.; Tao, G.; An, S.; Makur, A.; Ma, S.; and Zhang, X. 2024. Exploring the Orthogonality and Linearity of Backdoor Attacks. In *2024 IEEE Symposium on Security and Privacy (SP)*, 225–225. IEEE Computer Society.
- Zhang, X.; Hu, H.; Ye, Q.; Bai, L.; and Zheng, H. 2025. MER-Inspector: Assessing Model Extraction Risks from An Attack-Agnostic Perspective. In *Proceedings of the ACM on Web Conference 2025, WWW 2025, Sydney, NSW, Australia*, 4300–4315. ACM.
- Zhang, X.; Zhao, J.; and LeCun, Y. 2015. Character-level convolutional networks for text classification. *Advances in neural information processing systems*, 28.
- Zheng, H.; Ye, Q.; Hu, H.; Fang, C.; and Shi, J. 2019. BDPL: A Boundary Differentially Private Layer Against Machine Learning Model Extraction Attacks. In Sako, K.; Schneider, S. A.; and Ryan, P. Y. A., eds., *Computer Security - ESORICS 2019, Part I*, volume 11735 of *Lecture Notes in Computer Science*, 66–83. Springer.
- Zheng, H.; Ye, Q.; Hu, H.; Fang, C.; and Shi, J. 2022a. Protecting Decision Boundary of Machine Learning Model With Differentially Private Perturbation. *IEEE Trans. Dependable Secur. Comput.*, 19(3): 2007–2022.
- Zheng, R.; Tang, R.; Li, J.; and Liu, L. 2022b. Data-free backdoor removal based on channel lipschitzness. In *European Conference on Computer Vision*, 175–191. Springer.
- Zhu, H.; Liang, S.; Hu, W.; Li, F.; Jia, J.; and Wang, S. 2024. Reliable Model Watermarking: Defending Against Theft without Compromising on Evasion. *arXiv preprint arXiv:2404.13518*.
- Zhu, R.; Tang, D.; Tang, S.; Wang, X.; and Tang, H. 2023. Selective amnesia: On efficient, high-fidelity and blind suppression of backdoor effects in trojaned machine learning models. In *2023 IEEE Symposium on Security and Privacy (SP)*, 1–19. IEEE.

Appendix

A. Proof

A.1. Proof of Model Extraction Attack (MEA) Failure Condition in Theorem 1

Proof. Assuming X_q^T has a pseudoinverse $(X_q^T)^{-1}$, the copy model's parameters θ_{mea} estimated by queries are

$$\theta_{mea} = Y_q^T (X_q^T)^{-1}. \quad (9)$$

The performance of θ_{mea} on a domain sample $\mathbf{x}^T \in X$ is

$$\mathbf{y}_{mea}^T = \theta_{mea} \mathbf{x}^T = Y_q^T (X_q^T)^{-1} \mathbf{x}^T. \quad (10)$$

The right term in Equation 10 performs a weighted sum of the columns of Y_q^T , i.e.,

$$\mathbf{y}_{mea}^T = [\mathbf{y}_{q1}^T, \dots][w_1, \dots]^T = \sum w_i \mathbf{y}_{qi}^T, \quad (11)$$

where \mathbf{y}_{qi}^T is the i -th column in Y_q^T and w_i is a weight scalar. Since any $\mathbf{y}^T \in Y^T$ is orthogonal to all $\mathbf{y}_q^T \in Y_q^T$, it cannot be equal to any \mathbf{y}^T , i.e., $\mathbf{y}_{mea}^T \neq \mathbf{y}$. \square

A.2. Proof of Lower Bound on NTK Cross-Kernel Norm by Representation Entanglement (RE) in Theorem 2

Proof. Following the neural tangent kernel (NTK) theory (Bennani, Doan, and Sugiyama 2020), we assume the model $F: \mathbb{R}^d \rightarrow \mathbb{R}$. $\|\phi(X_w)\phi(X)^T\|_2$ can be expressed at the layer level:

$$\|\phi(X_w)\phi(X)^T\|_2 = \left\| \sum_{l \in L} \nabla_{\theta^l} F(X_w) \cdot \nabla_{\theta^l} F(X)^T \right\|_2. \quad (12)$$

Besides, $\nabla_{\theta^l} F(\cdot)$ can be calculated by the following equation:

$$\nabla_{\theta^l} F(\cdot) = \delta_l(\cdot) F_{\theta^{l-1}}(\cdot), \quad (13)$$

where $\delta_l(X_w) = \text{Diag}(\sigma'(z_l)) \cdot \theta^{l+1T} \cdot \delta_{l+1}$. For the output layer L , $\delta_L = I$. σ is the activation function. z_l denotes the output of the l -th linear layer, i.e., $F_{\theta^l}(X) = \sigma(z_l)$. σ' is the derivative of the activation function. For ReLU, σ' consists of 0 or 1.

Assuming that the feature map $\phi(\cdot)$ used in computing RE is defined as the mean vector. Then, Equation 12 can be further written as

$$\begin{aligned} & \|\phi(X_w)\phi(X)^T\|_2 \\ &= \left\| \sum_{\mathbf{x}_w \in X_w} \sum_{\mathbf{x} \in X} \sum_{l \in \{L\}} \delta_l(\mathbf{x}_w) \underbrace{F_{\theta^l}(\mathbf{x}_w) F_{\theta^l}(\mathbf{x})^T}_{\in \mathbb{R}^{1 \times 1}} \delta_l(\mathbf{x})^T \right\|_2 \\ &= \sum_{\mathbf{x}_w \in X_w} \sum_{\mathbf{x} \in X} |F_{\theta^l}(\mathbf{x}_w) F_{\theta^l}(\mathbf{x})^T| \underbrace{\left\| \sum_{l \in \{L\}} \delta_l(\mathbf{x}_w) \delta_l(\mathbf{x})^T \right\|_2}_{\gamma(\mathbf{x}_w, \mathbf{x})} \end{aligned} \quad (14)$$

Let $\gamma_{\min} = \min_{\mathbf{x}_w \in X_w, \mathbf{x} \in X} \gamma(\mathbf{x}_w, \mathbf{x})$. We note that $\gamma_{\min} \geq 1$ always holds, as formally stated in Theorem 3, which will be proved later. Then from Equation 14, we can derive:

$$\begin{aligned} \|\phi(X_w)\phi(X)^T\|_2 &\geq \sum_{\mathbf{x}_w \in X_w} \sum_{\mathbf{x} \in X} \gamma_{\min} \|F_{\theta^l}(\mathbf{x}_w) F_{\theta^l}(\mathbf{x})^T\| \\ &\geq \left\| \left(\sum_{\mathbf{x}_w \in X_w} F_{\theta^l}(\mathbf{x}_w) \right) \left(\sum_{\mathbf{x} \in X} F_{\theta^l}(\mathbf{x}) \right)^T \right\|_2 \\ &= \underbrace{N_w N}_{\Gamma} \mathcal{RE}(F_{\theta}; X_w, X) \end{aligned} \quad (15)$$

Therefore, let $\Gamma = N_w N$, and we can deduct that:

$$\|\phi(X_w)\phi(X)^T\|_2 \geq \Gamma \cdot \mathcal{RE}(F_{\theta}; X_w, X) \quad (16)$$

\square

Theorem 3. For any inputs $\mathbf{x}_w \in X_w, \mathbf{x} \in X$,

$$\gamma_{\min} \geq 1, \quad \text{where } \gamma(\mathbf{x}_w, \mathbf{x}) = \left\| \sum_{l=1}^L \delta_l(\mathbf{x}_w) \delta_l(\mathbf{x})^T \right\|_2 \quad (17)$$

Proof. Each layer contributes a positive semi-definite (PSD) matrix:

$$\delta_l(\mathbf{x}_w) \delta_l(\mathbf{x})^T \succeq 0 \quad \forall l \in \{1, \dots, L\}, \quad (18)$$

where the PSD property follows from the matrix outer product structure. The output layer ($l = L$) contribution is:

$$\delta_L(\mathbf{x}_w) \delta_L(\mathbf{x})^T = I I^T = I \quad (19)$$

As a result, for the complete sum, the PSD property guarantees spectral norm accumulation:

$$\sum_{l=1}^L \delta_l(\mathbf{x}_w) \delta_l(\mathbf{x})^T \succeq I + \underbrace{\sum_{l=1}^{L-1} \delta_l(\mathbf{x}_w) \delta_l(\mathbf{x})^T}_{\succeq 0} \succeq I. \quad (20)$$

Therefore, the spectral norm of this PSD matrix satisfies

$$\left\| \sum_{l=1}^L \delta_l(\mathbf{x}_w) \delta_l(\mathbf{x})^T \right\|_2 \geq \text{largest eigenvalue of } I = 1, \quad (21)$$

with equality only if all hidden layer contributions vanish. Since gradient signals in practical networks always contain non-zero backward passes through hidden layers, the inequality is strict ($\gamma_{\min} > 1$) for $L > 1$. \square

A.3. Derivation of the CD² Loss in Equation 6

Starting from neural tangent kernel (NTK) theory (Bennani, Doan, and Sugiyama 2020), which assumes the model $F: \mathbb{R}^d \rightarrow \mathbb{R}$, e.g., F is a binary classifier, we approximate the output of the MEA-extracted copy model \hat{F} by a linearized model around the victim model F :

$$\hat{F}(\mathbf{x}) = \phi(\mathbf{x}) \Delta \theta + F_0(\mathbf{x}), \quad \text{where } \phi(\mathbf{x}) = \nabla_{\theta} F(\mathbf{x}), \quad (22)$$

and $\Delta \theta$ is derived from fine-tuning data (X_q, Y_q) :

$$\Delta \theta = \phi(X_q)^T \left[\phi(X_q) \phi(X_q)^T + \lambda I \right]^{-1} \tilde{\mathbf{y}}, \quad (23)$$

with $\tilde{\mathbf{y}} = F(X_q) - F_0(X_q)$ representing residual outputs. Considering the closeness of query set X_q to the domain dataset X , we approximate X_q with X .

To ensure pairwise consistency among watermark representations after distortion, we minimize:

$$L_{\text{CD}^2} = \frac{1}{N_w^2} \sum_{\mathbf{x}_i, \mathbf{x}_j \in D_w} |(\phi(\mathbf{x}_j) - \phi(\mathbf{x}_i)) \Delta \theta|. \quad (24)$$

Applying singular value decomposition (SVD) to domain gradients, we obtain $\phi(X) = U \Sigma V^T$. Thus, Equation 24 reduces to minimizing the projection onto principal distortion directions represented by columns of V :

$$L_{\text{CD}^2} = \frac{1}{N_w^2} \sum_{\mathbf{x}_i, \mathbf{x}_j \in D_w} |(\phi(\mathbf{x}_j) - \phi(\mathbf{x}_i)) V \Sigma [\Sigma^2 + \lambda I]^{-1} U^T \tilde{\mathbf{y}}|. \quad (25)$$

For computational simplicity, we further restrict optimization to the output layer L , giving the simplified loss:

$$L_{CD^2} = \frac{1}{N_w^2} \sum_{\mathbf{x}_i, \mathbf{x}_j \in \mathcal{D}_w} |(\nabla_{\theta^L} F(\mathbf{x}_j) - \nabla_{\theta^L} F(\mathbf{x}_i)) V_{\theta^L}|. \quad (26)$$

Considering $\nabla_{\theta^L} F(\cdot) = F_{\theta^{L-1}}(\cdot)$, the final simplified form becomes:

$$L_{CD^2} = \frac{1}{N_w^2} \sum_{\mathbf{x}_i, \mathbf{x}_j \in \mathcal{D}_w} |(F_{\theta^{L-1}}(\mathbf{x}_j) - F_{\theta^{L-1}}(\mathbf{x}_i)) V_{\theta^L}|. \quad (27)$$

Empirical evidence in Appendix B.2 (Xiao et al. 2025) verifies that the direction represented by V_{θ^L} aligns closely with the principal component directions of representation distortion induced by MEA, validating our theoretical assumptions.

B. Experimental Validation

B.1. Experimental Validation for the Relationship of Representation Entanglement (RE) and MEA Transferability

We empirically validate the relationship between the metric representation entanglement (\mathcal{RE} in Definition 1) and MEA transferability across a range of black-box watermark and backdoor methods. \mathcal{RE} is simplified by defining ψ as the mean vector. MEA transferability is quantified by the watermark success rate (WSR) in the extracted copy model (see Equation 31). In addition to the watermark benchmarks EWE (Jia et al. 2021), MEA-Defender (Lv et al. 2024) and MBW (Kim et al. 2023), we include four different types of backdoor attacks to examine the effect of watermark sample types on MEA transferability, including sticker-type BadNet (Gu et al. 2019), Blend (Chen et al. 2017), invisible-type WaNet (Nguyen and Tran 2021), and composite backdoors (Lin et al. 2020). The \mathcal{RE} of backdoor tasks is influenced by their poison rates (Min et al. 2023), with lower rates potentially increasing \mathcal{RE} . Therefore, we use minimal poison rates for each backdoor attack, as further reduction fails to embed. We adopt ActiveThief (Pal et al. 2020) as the MEA algorithm. Detailed experimental settings are described in Appendix D (Xiao et al. 2025).

Results. As shown in Figure 6, there is a clear positive correlation between \mathcal{RE} and the copy model’s WSR. Once \mathcal{RE} is lower than 0.3, WSR drops sharply for backdoor-type tasks. Interestingly, the type of watermark data has a limited impact on WSR, as even sticker-type BadNet achieves high MEA transferability when its \mathcal{RE} is sufficiently large.

B.2. Empirical Validation of Distortion Directions Deduced by CD^2 Loss in Equation 6

In this section, we empirically validate the theoretical objective derived from CD^2 optimization. The term $(F_{\theta^{L-1}}(\mathbf{x}_j) - F_{\theta^{L-1}}(\mathbf{x}_i))$ in Equation 6 can be interpreted as the representation distance between two watermark samples \mathbf{x}_i and \mathbf{x}_j , then V_{θ^L} characterizes **the distortion directions** that influence this distance. Intuitively, Equation 6 minimizes the projection of this distance onto these directions, thereby reducing vulnerability to perturbations.

In Equation 6, V_{θ^L} is defined as the principal component decomposition of the domain dataset’s representations.

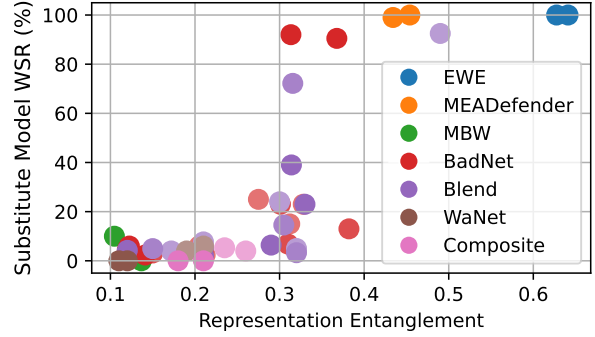


Figure 6: WSR of the copy model versus representation entanglement. For each backdoor task, the color intensity indicates the poison rate, with values of 0.001, 0.002, and 0.003 for BadNet and Blend, and 0.05 and 0.1 for WaNet and Composite, as lower rates fail to embed.

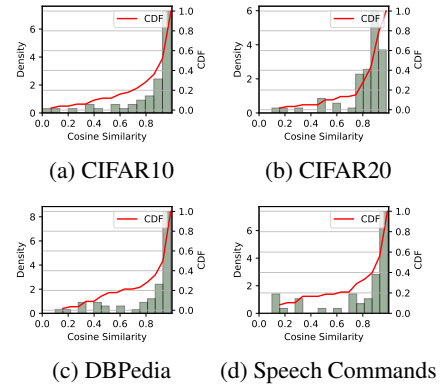


Figure 7: Histogram of the domain class PC cosine similarity between original and deformed representations in MEA, with statistics collected over 3-5 trials.

In other words, the distortion directions correspond to the principal directions (PCs) of domain representations. These distortions may result from either MEA or learning-induced removal attacks.

To validate this, we compare the domain PCs of victim models with those of (1) copy models extracted via MEA and (2) models after learning-induced removal. Note that PCs are computed separately for each class to capture fine-grained alignment. The results are shown in Figure 7 and Figure 8, respectively. These histograms report the cosine similarity of last-layer PCs before and after distortion. A higher concentration of values near 1 indicates a more substantial alignment between the updated directions and the PCs of the domain dataset’s representations, which supports the deduction in Equation 6 that these PCs are indeed the distortion directions that affect the watermark data. Our results show that over 80% of cosine similarities exceed 0.6 across most settings, except for I-BAU. This provides strong empirical support for the CD^2 -derived theory that **the principal directions of domain representations are the dominant distortion directions**.

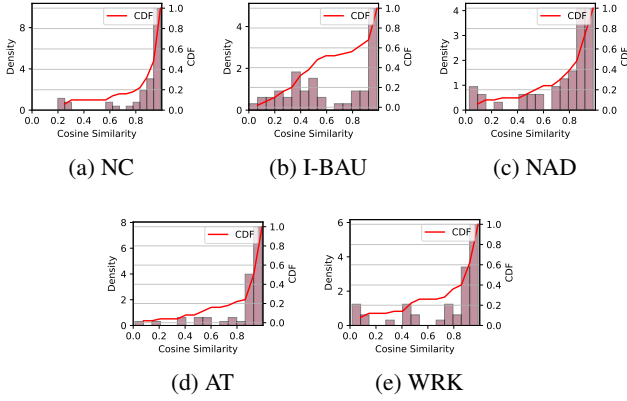


Figure 8: Histogram of domain class principal component cosine similarities between original and deformed representations under **learning-based removal attacks**, averaged over five independent trials.

B.3. Empirical Validation of Predictable Deformation Labels via Principal Component Alignment

In Figure 4a, the deformation labels consistently transfer from 0 to 3. However, during removal attacks, deformation labels may vary or span multiple classes due to unknown and uneven perturbation strengths across output dimensions.

Nevertheless, we posit that deformation labels are not arbitrary but can be predicted. To substantiate this claim, we first analyze the class-wise interactions during watermark removal. As established in Appendix B.2 (Xiao et al. 2025), the distortions introduced during removal predominantly align with the principal component (PC) directions of each domain class’s representations.

We hypothesize that if the PC directions of a domain class are approximately opposite to those of the watermark-assigned class (computed from the domain dataset), this domain class is more likely to dominate the distortion processes. Consequently, it may absorb the watermark decision boundary, thereby becoming the resulting deformation label. This hypothesis is formalized as follows:

Proposition 1 (Deformation Label Formation). *Let the following be given:*

- C_d : A candidate domain class, with its first principal component direction denoted by \mathbf{v}_d ,
- C_w : The watermark-assigned class, with its first principal component direction (computed from the domain dataset) denoted by \mathbf{v}_w ,
- $\mathcal{S}(\mathbf{v}_d, \mathbf{v}_w) := \cos(\mathbf{v}_d, \mathbf{v}_w)$: The cosine similarity between \mathbf{v}_d and \mathbf{v}_w ,

then C_d emerges as the deformation label under removal perturbation if the following condition holds:

$$\mathcal{S}(\mathbf{v}_d, \mathbf{v}_w) = \min_{C \sim D} [\mathcal{S}(\mathbf{v}_C, \mathbf{v}_w)], \text{ \& } \mathcal{S}(\mathbf{v}_d, \mathbf{v}_w) < 0, \quad (28)$$

where D is the domain class distribution. This condition indicates geometric opposition in principal subspaces.

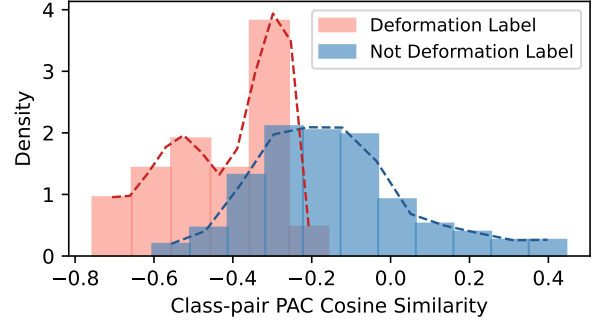


Figure 9: *Density* histogram of PC cosine similarity between classes contains watermarks and others. The ratio of deformation labels to non-deformation labels is 1 : 9.

We validate Proposition 1 by empirically analyzing the cosine similarity between the PCs of domain classes assigned watermark tasks and those of their corresponding deformation labels after WRK. Figure 9 presents the result, which indicates that deformation labels consistently exert opposing stretching, with negative cosine similarity to the watermark label. In contrast, the PCs of non-deformation domain classes exhibit higher orthogonality with the target class assigned to the watermark task. Therefore, to ensure deformation label consistency, the watermark label should be fine-tuned or chosen to have **only one possible deformation label**, as demonstrated with class 0 in the experiments in the section titled *Verify CFW with Intra-class Clustering*.

C. Algorithm of Watermark Removal Attack

Algorithm 1 presents the Watermark Removal Attack (WRK) in algorithmic form.

Algorithm 1: Watermark Removal Attack (WRK)

Input: Stolen copy model F_s with parameters θ , domain-relevant subset D_d , subset ratio $\rho \in (0, 1]$, noise magnitudes ϵ ,
Output: Watermark removed model $F_{s, \text{wrk}}^L$
1: Extract final layer weights: $\theta_{\text{ini}}^L \leftarrow \theta^L$
2: Sample subset: $D'_d \leftarrow \text{RANDOMSAMPLE}(D_d, \rho)$
3: **for** each $x \in D'_d$ **do**
4: Compute perturbation: $\delta_x \leftarrow \text{FGSM}(F_\theta, x, \epsilon)$
5: Generate adversarial example: $\tilde{x} \leftarrow \text{Clip}(x + \delta_x)$
6: Assign random label: $y \sim \mathcal{U}(\{1, \dots, K\})$
7: Add to the poisoned set: $D_p \leftarrow D_p \cup \{(\tilde{x}, y)\}$
8: **end for**
9: Combine datasets: $D_{\text{train}} \leftarrow D_d \cup D_p$
10: Initialize θ^L
11: Fine-tune model: $F_{s, \text{wrk}}^L \leftarrow \text{argmin}_\theta L_{\text{wrk}}$ ▷ Equation 3
12: **return** $F_{s, \text{wrk}}^L$

D. Experimental Setup Details

D.1. WRK Experiment Setup Details

Black-box Watermark and Backdoor Benchmarks. We benchmark four black-box model watermarks against MEAs: EWE (Jia et al. 2021), MBW (Kim et al. 2023),

MEA-Defender (MEA-D) (Lv et al. 2024), and a typical backdoor methods **Blend** (Chen et al. 2017). Since these watermarking methods are specifically designed for image classification, we conduct experiments on the CIFAR-10 (Krizhevsky, Hinton et al. 2009) dataset with ResNet18 (He et al. 2016) and on ImageNette (Howard 2019) with ResNet50 (He et al. 2016). All experiments follow their original frameworks with optimized settings. In detail, for EWE and MEA-Defender, the watermark datasets comprise 5% and 10% of the training data, respectively. MBW follows its original setups, using 10 watermark samples. Blend adopts a small watermark dataset ratio of 0.3%, which contributes to increasing its representation entanglement (RE).

To assess the broader applicability of WRK, we evaluate its removal performance on other backdoors: **WaNet** (Nguyen and Tran 2021) and **composite backdoor** (Lin et al. 2020). These backdoor methods are excluded from watermark evaluation since they do not survive model extraction.

Removal-related Setups. We compare WRK against nine recent removal methods that have official implementations and are not limited by architectural assumptions (*e.g.*, batch normalization). These methods fall into three categories: **reversion-based** (NC (Wang et al. 2019), I-BAU (Zeng et al. 2022), DTI-DBF (Xu et al. 2023)), **neuron pruning** (FP (Liu, Dolan-Gavitt, and Garg 2018), CLP (Zheng et al. 2022b)), and **learning-induced forgetting** (NAD (Li et al. 2021), SEAM (Zhu et al. 2023), FST (Min et al. 2023)). In addition, Adversarial Training (AT) (Alexey, Ian, and Samy 2016) is included as a baseline.

All removal methods use a domain dataset comprising 5% of the original training set for CIFAR-10 and 10% for ImageNette, and model utility degradation is constrained to within 2% where applicable. For WRK, the noise magnitude ϵ is set to $1.5_{-0.5}^{+0.5}$ (after normalization) and the coefficient for weight-shifting regularization α is set to $0.05_{-0.02}^{+0.05}$. The optimizer in WRK is set to SGD (Bottou 2010) with learning rate 0.001 for CIFAR-10 and $0.0003_{-0.0002}^{+0.0002}$ for Imagenette. **Model Extraction Attack (MEA) Settings.** Considering the threat model assumes the adversary prepares a limited number of domain samples for removal attacks, we evaluate two MEA benchmarks: MExMI (Xiao et al. 2022), which emphasizes domain samples to enhance MEA performance, and ActiveThief (Pal et al. 2020). To ensure meaningful attack results, the query data pool is supplemented with out-of-domain datasets from ImageNet (Deng et al. 2009). Both methods use a query budget of 25,000 for CIFAR-10 and 5,000 for ImageNette, which are consistent with their original scales.

Metrics. The calculations for these metrics are as follows:

Accuracy (ACC). For the model F and the test dataset D_t of size N_t ,

$$\text{ACC}(F, D_t) = \frac{100}{N_t} \sum_{(\mathbf{x}, y) \in D_t} \mathbf{1}(F(\mathbf{x}) = y)\%, \quad (29)$$

where $\mathbf{1}(\cdot)$ denotes the indicator function.

Fidelity (FID). For the copy model F_s and the victim model F_v ,

$$\text{FID}(F_s, F_v) = \frac{100}{N_t} \sum_{(\mathbf{x}, y) \in D_t} \mathbf{1}(F_s(\mathbf{x}) = F_v(\mathbf{x}))\%. \quad (30)$$

Watermark Success Rate (WSR). For the model F and the watermark dataset D_w of size N_w and the watermark label y_w ,

$$\text{WSR}(F, D_w | y_w) = \frac{100}{N_w} \sum_{\mathbf{x} \in D_w} \mathbf{1}(F(\mathbf{x}) = y_w)\%. \quad (31)$$

Implementation Details. All results are averaged over five independent runs with different random seeds to stimulate uncertainty, with variation bounds shown as **maximum** observed deviations. The implementation runs on a Windows workstation equipped with two NVIDIA RTX 4090 GPUs.

D.2. CFW Experiment Setup Details

Dataset Descriptions. CIFAR-10 and CIFAR-20 each contain 50,000 training and 10,000 test images (3-channel 32x32 pixels); CIFAR-10 has 10 labels, while CIFAR-20 uses 20 superclasses from CIFAR-100. ImageNette contains higher-resolution images which we resize to 128x128 pixels, comprising 9,469 training instances and 3,925 test samples across 10 categories. DBpedia includes 560,000 samples categorized into 14 classes. Google Speech Commands comprises over 105,000 utterances of 35 words from various speakers, organized into 12 classes.

Class-Feature Watermark (CFW) Settings. The CFW dataset is created by selecting multiple out-of-domain (OOD) data types and assigning them to the same label. To constrain feature complexity, the watermark dataset is limited to 0.2%–0.3% of the domain dataset, except for Imagenette, which uses 1.5%. For CIFAR-10, 150 samples are taken from 10 non-overlapping classes in CIFAR-100. For CIFAR-20, 150 samples are selected from 4 classes in ImageNet (Deng et al. 2009). For ImageNette, 30 samples are drawn from 10 ImageNet classes that do not overlap with those in ImageNette, even at the superclass level. For DBpedia, 300 CFW samples are LLM-generated to mimic DBpedia’s style while remaining semantically OOD, and for Google Speech Commands, 300 samples are taken from 4 classes within the ‘unknown’ category. The weighting factors λ_1 is set to $0.5_{-0.3}^{+0.3}$, and $\lambda_2 > 0$ is set to $0.0003_{-0.0002}^{+0.0005}$.

Model Extraction Attack (MEA) Settings. The MEA query pools of MExMI (Xiao et al. 2022) and ActiveThief (Pal et al. 2020) consist of both in-domain and out-of-distribution (OOD) samples. **Notably, the OOD samples used in MEA are entirely disjoint from the CFW dataset, and even the classes do not overlap.** For instance, in the CIFAR-20 experiment, the adversarial pool consists of the first 100 ImageNet classes, while the CFW data is drawn from classes 530 to 533. Following the WRK experiment setups, the domain subset constitutes 5% of the training dataset and is also used for removal attacks. For image tasks CIFAR-10 and CIFAR-20, the OOD samples are from ImageNet32 (Deng et al. 2009), with a query budget of 25,000. For ImageNette, OOD samples are selected from ImageNet with a budget of 5,000. For DBpedia, the pool is AG News dataset (Zhang, Zhao, and LeCun 2015), with a budget of 50,000, and for Speech Commands, the pool includes classes from version 0.02 absent in version 0.01, with a budget of 100,000. The copy model architectures match the victim models in default experiments. Further, Appendix E.10 (Xiao et al. 2025) reports cross-experiments

using ResNet-18, MobileNetV2 (Sandler et al. 2018), and VGG19-BN to evaluate the impact of architectures on CFW. **Metrics.** Since CFW is verified with clustering, in addition to WSR, we introduce the following two metrics.

Intra-class Variance (Intra Var, Var). This metric calculates the mean squared distance from each sample to its class centroid in the t-SNE (Van der Maaten and Hinton 2008) reduced representation space (normalized to $[-100, 100]$). For a model F and the watermark dataset D_w , it is computed as:

$$\text{Var}(F, D_w) = \frac{1}{N_w} \sum_{\mathbf{x} \in D_w} \|\text{t-SNE}(F_{\theta^L}(\mathbf{x})) - \mu\|_2^2, \quad (32)$$

where μ is the centroid of the reduced representations of watermark tasks, $\mu = \mathbf{E}(\text{t-SNE}(F_{\theta^L}(D_w)))$.

Label Clustering (WSR_{LC}). This metric evaluates the clustering behavior on the watermark label y_w and the deformation label y_{deform} :

$$\text{WSR}_{\text{LC}} = \text{WSR}(F, D_w | y_w) + \text{WSR}(F, D_w | y_{\text{deform}}). \quad (33)$$

E. Supplementary Experiments

E.1. WRK Performance on Imagenette

We extend our experiments of WRK to ImageNette with ResNet50. Table 6 confirms that EWE and MEA-Defender transfer well under MEXMI and ActiveThief, whereas MBW does not. Blend is omitted because it never transfers on this dataset.

Table 5 compares WRK with existing removal methods on victim models. In detail, reversion-type removal, neuron pruning and learning-induced forgetting baselines leave high WSRs ($\leq 70\%$) on strong watermarks such as EWE. Yet WRK cuts WSRs below 11% for every watermark while keeping accuracy high. WRK also cleanses the backdoors, reducing the success rate of WaNet to 0% WSR and Composite to 5.96%. These results confirm that WRK is still effective on a high-resolution image benchmark.

E.2. Removal Attack Results on Copy Models

We evaluate the effectiveness of WRK and benchmark removal attacks on copy models extracted via MEA. Table 7 presents the removal performance on copy models, which complements the victim model results shown in Table 2. Compared to victim models, copy models generally exhibit similar watermark removal trends, with WRK consistently achieving low WSRs across all watermarking methods while maintaining model accuracy.

E.3. Evaluation of WRK Variants

We evaluate the individual impact of WRK’s two critical mechanisms: *Boundary Reshaping* (BR) and the output-layer weight shift inspired by the FST framework (Min et al. 2023). We also compare BR against typical adversarial training (AT) (Alexey, Ian, and Samy 2016) to highlight its necessity. The ablation study includes two WRK variants: *BR only* and *FST only*, each disabling one mechanism. Table 8 presents the results.

We have the following observations. First, adversarial training (AT) (Alexey, Ian, and Samy 2016) is largely ineffective against most watermark and backdoor methods,

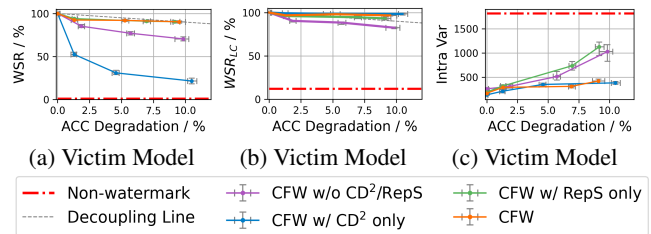


Figure 10: Watermark decoupling curves of CFW on victim models. Vertical lines indicate error bars.

with limited impact only on EWE and MBW, and consistently weaker than *BR only*. Second, for EWE, MBW, and WaNet, both *BR only* and full WRK achieve strong removal, indicating BR’s primary role in handling noise-type triggers, while FST provides complementary benefits. In contrast, for MEA-Defender, Blend, and Composite backdoors, adding BR to FST substantially enhances removal. This indicates that BR also benefits the removal of non-noise triggers. Overall, BR and FST serve as orthogonal yet mutually beneficial components.

E.4. Sensitivity Analysis of WRK Hyperparameters

We evaluate the sensitivity of WRK to its two key hyperparameters. The first is ϵ , which controls the magnitude of adversarial perturbations used in boundary reshaping. The second is α , which is the coefficient of the parameter-shift regularization term in Eq. (3). We vary $\epsilon \in \{0.01, 0.03, 0.05\}$ and $\alpha \in \{0.05, 1.0, 1.5\}$ to assess their impact on model accuracy (ACC) and watermark success rate (WSR) across EWE and MEA-Defender watermarks.

Table 9 presents the results. For EWE, $\epsilon = 0.03$ with $\alpha = 1.0$ achieves optimal balance. This configuration reduces WSR to 8.75% and maintains 91.44% accuracy. For MEA-Defender, larger ϵ is required. At $\epsilon = 0.03$, $\alpha = 1.5$ yields WSR of 7.64%. Overall, WRK demonstrates moderate sensitivity within the tested ranges.

E.5. Watermark Decoupling Curves on Victim Models

Figure 10 presents supplementary results showing the decoupling behavior of Class-Feature Watermarks (CFW) on victim models under WRK removal.

E.6. Comparing WSR and WSR_{LC} for Watermark Baselines and CFW

We compare the resilience of WSR and WSR_{LC} between CFW and representative baseline watermarks. Recall that WSR_{LC} is defined as the sum of WSRs over watermark and deformation labels, providing clustering-based evidence for ownership verification.

Table 10 reports WSR values for CFW across five datasets. On victim models, CFW maintains perfect WSR before WRK removal. After WRK attacks, WSR remains above 92% on victim models. On copy models extracted via MEA, WSR ranges from 82.67% to 93.12% before removal,

Table 5: Performance of WRK and Benchmark Removal Attack on ImageNette

Removal Method	None		Reversion-type Removal						Neuron Pruning				Learning-induced Forgetting							
			NC		I-BAU		BTI-DBF		CLP		FP		NAD		SEAM		FST		WRK(Ours)	
Metrics/%	ACC	WSR	ACC	WSR	ACC	WSR	ACC	WSR	ACC	WSR	ACC	WSR	ACC	WSR	ACC	WSR	ACC	WSR	ACC	WSR
EWE	86.42 _{±0.08}	99.95 _{±0.08}	84.76 _{±0.44}	99.61 _{±0.05}	86.28 _{±0.05}	99.12 _{±0.18}	85.92 _{±0.42}	92.59 _{±0.06}	85.89 _{±0.08}	98.75 _{±0.25}	84.52 _{±0.42}	98.72 _{±0.22}	84.39 _{±0.46}	98.56 _{±0.34}	83.25 _{±0.02}	99.22 _{±0.13}	84.03 _{±0.40}	69.14 _{±0.33}	84.35 _{±0.37}	10.55 _{±0.74}
MBW	76.01 _{±1.13}	100.00 _{±0.00}	75.53 _{±1.12}	100.00 _{±0.00}	74.85 _{±1.15}	6.00 _{±0.00}	74.21 _{±1.35}	2.00 _{±0.00}	72.03 _{±1.44}	46.00 _{±3.04}	74.26 _{±1.39}	84.00 _{±0.00}	74.14 _{±1.19}	4.00 _{±0.00}	79.15 _{±1.08}	0.00 _{±0.00}	78.85 _{±1.00}	8.00 _{±0.00}	79.39 _{±0.08}	6.00 _{±0.00}
MEA-D	74.36 _{±0.25}	79.54 _{±0.06}	73.51 _{±0.82}	70.11 _{±1.24}	73.19 _{±0.82}	33.88 _{±0.06}	73.42 _{±0.79}	14.34 _{±0.84}	72.53 _{±0.06}	77.82 _{±0.74}	72.97 _{±0.44}	78.84 _{±0.29}	73.25 _{±0.06}	24.82 _{±1.38}	73.95 _{±0.03}	16.97 _{±0.13}	72.93 _{±0.04}	36.84 _{±0.46}	74.06 _{±0.03}	3.62 _{±0.81}
Blend	82.59 _{±0.05}	90.52 _{±1.25}	N/A	N/A	82.36 _{±0.48}	82.52 _{±1.32}	80.52 _{±0.75}	56.75 _{±0.51}	80.53 _{±0.76}	81.67 _{±1.65}	83.17 _{±0.31}	80.76 _{±1.09}	80.67 _{±0.46}	77.73 _{±1.35}	80.27 _{±0.05}	19.66 _{±0.22}	80.35 _{±0.02}	6.35 _{±1.85}	80.56 _{±0.45}	3.53 _{±0.91}
WaNet	87.16 _{±0.45}	99.15 _{±0.25}	85.54 _{±0.36}	43.53 _{±1.35}	87.28 _{±0.40}	0.15 _{±0.16}	85.17 _{±0.55}	0.31 _{±0.31}	86.68 _{±0.34}	99.89 _{±0.05}	85.86 _{±0.00}	4.85 _{±1.34}	85.27 _{±0.60}	0.36 _{±0.36}	84.94 _{±0.74}	0.42 _{±0.42}	85.24 _{±0.33}	0.83 _{±0.83}	86.89 _{±0.30}	0.25 _{±0.25}
Composite	86.78 _{±0.30}	94.14 _{±0.05}	84.70 _{±0.05}	82.80 _{±1.29}	85.15 _{±0.40}	73.45 _{±1.67}	83.49 _{±0.08}	11.18 _{±0.20}	86.88 _{±0.10}	92.87 _{±0.09}	84.32 _{±0.40}	98.60 _{±0.10}	84.68 _{±0.70}	49.20 _{±1.18}	86.19 _{±0.05}	3.36 _{±0.05}	84.61 _{±0.04}	0.59 _{±0.10}	86.19 _{±0.25}	5.96 _{±0.85}

N/A indicates that NC does not identify any suspicious class and thus does not perform removal.

Table 6: Performance of Existing Black-box Watermarks on ImageNette

Method	Non-WM		Victim Model		Copy Model			
	ACC	WSR	ACC	WSR	MEA	ACC	FID	WSR
EWE	88.12 _{±0.15}	14.29 _{±3.32}	86.42 _{±0.38}	99.95 _{±0.08}	MEXMI 83.53 _{±0.02}	83.63 _{±0.00}	60.16 _{±2.73}	
					ActiveThief 81.54 _{±0.00}	81.96 _{±0.75}	58.79 _{±2.00}	
MBW	88.12 _{±0.15}	8.00 _{±0.00}	76.01 _{±1.13}	100.00 _{±0.00}	MEXMI 72.85 _{±0.53}	83.05 _{±0.79}	0.00 _{±0.00}	
					ActiveThief 70.16 _{±0.02}	79.55 _{±0.00}	0.00 _{±0.00}	
MEA-D	88.12 _{±0.15}	1.73 _{±0.44}	74.36 _{±0.75}	79.54 _{±0.05}	MEXMI 71.87 _{±0.08}	80.66 _{±0.82}	72.81 _{±0.70}	
					ActiveThief 68.86 _{±0.10}	78.42 _{±1.15}	67.70 _{±0.95}	

Non-WM denotes the abbreviation for non-watermark.

Table 7: Performance of WRK and benchmark removal attacks on copy models. Comp. denotes the abbreviation for composite backdoor. N/A indicates that NC does not identify any suspicious class and thus does not perform removal.

Removal	EWE		MBW		MEA-D		Blend	
	ACC	WSR	ACC	WSR	ACC	WSR	ACC	WSR
None	89.15 _{±0.48}	99.65 _{±0.35}	71.32 _{±1.30}	10.00 _{±0.00}	82.15 _{±0.31}	99.20 _{±0.15}	89.97 _{±0.41}	39.44 _{±1.26}
NC	88.99 _{±0.32}	96.67 _{±0.35}	70.33 _{±1.05}	0.00 _{±0.00}	82.13 _{±0.35}	75.54 _{±1.25}	88.15 _{±0.25}	1.49 _{±0.31}
I-BAU	88.35 _{±0.18}	99.15 _{±0.05}	75.16 _{±0.47}	0.00 _{±0.00}	83.56 _{±0.11}	86.67 _{±1.02}	88.33 _{±0.42}	35.85 _{±1.47}
BTI-DBF	87.05 _{±0.23}	10.21 _{±0.79}	70.32 _{±0.88}	0.00 _{±0.00}	80.21 _{±0.59}	20.35 _{±0.65}	87.56 _{±0.28}	3.15 _{±1.45}
CLP	68.33 _{±1.12}	99.98 _{±0.01}	67.67 _{±3.40}	10.00 _{±0.00}	63.47 _{±6.35}	98.35 _{±0.12}	71.66 _{±0.40}	69.81 _{±5.75}
FP	87.75 _{±0.35}	81.67 _{±3.85}	74.35 _{±0.98}	0.00 _{±0.00}	83.05 _{±0.14}	62.10 _{±2.40}	88.17 _{±0.35}	41.53 _{±9.60}
NAD	87.46 _{±0.69}	99.58 _{±0.22}	72.56 _{±1.02}	0.00 _{±0.00}	76.25 _{±0.35}	97.40 _{±0.25}	88.17 _{±0.28}	20.75 _{±4.55}
SEAM	88.57 _{±0.35}	10.23 _{±1.25}	70.59 _{±0.65}	4.00 _{±0.00}	80.15 _{±1.15}	35.54 _{±8.41}	88.32 _{±0.32}	5.45 _{±3.40}
FST	87.25 _{±0.42}	5.31 _{±0.24}	69.80 _{±0.34}	4.00 _{±0.00}	79.79 _{±0.95}	5.20 _{±1.25}	87.79 _{±0.75}	14.15 _{±5.65}
WRK	88.51 _{±0.39}	5.88 _{±1.28}	71.11 _{±0.45}	2.00 _{±0.00}	81.35 _{±0.38}	4.76 _{±1.22}	88.75 _{±0.27}	2.81 _{±0.38}

Table 8: Performance of WRK Variants

Variants	AT		BR only		FST only		WRK	
	ACC	WSR	ACC	WSR	ACC	WSR	ACC	WSR
CIFAR-10								
EWE	90.49 _{±0.18}	22.89 _{±2.12}	91.32 _{±0.12}	12.30 _{±1.01}	89.96 _{±0.20}	23.55 _{±4.30}	91.44 _{±0.08}	8.75 _{±1.75}
MBW	82.06 _{±0.25}	10.00 _{±0.00}	83.35 _{±0.22}	0.00 _{±0.00}	83.17 _{±0.87}	6.00 _{±0.00}	82.50 _{±0.11}	4.00 _{±0.00}
MEA-D	85.90 _{±0.14}	81.44 _{±3.21}	86.50 _{±0.07}	72.15 _{±2.82}	86.08 _{±0.04}	6.78 _{±0.30}	85.46 _{±0.12}	7.64 _{±0.28}
Blend	92.25 _{±0.12}	85.02 _{±4.12}	92.11 _{±0.14}	45.20 _{±1.65}	92.48 _{±0.02}	57.51 _{±6.76}	92.40 _{±0.07}	9.80 _{±2.18}
WaNet	91.45 _{±0.12}	83.54 _{±3.14}	92.31 _{±0.11}	5.65 _{±0.00}	91.88 _{±0.04}	81.01 _{±0.40}	92.19 _{±0.09}	0.56 _{±0.25}
Composite	91.21 _{±0.16}	90.35 _{±2.44}	91.19 _{±0.19}	77.20 _{±1.12}	91.07 _{±0.30}	3.80 _{±0.30}	91.82 _{±0.15}	6.00 _{±0.30}
ImageNette								
EWE	86.15 _{±0.75}	84.89 _{±3.84}	86.01 _{±0.04}	19.21 _{±2.12}	84.03 _{±0.03}	69.14 _{±0.03}	84.35 _{±0.17}	10.55 _{±0.84}
MBW	79.14 _{±0.40}	6.00 _{±0.00}	77.94 _{±1.04}	4.00 _{±0.00}	78.85 _{±1.10}	8.00 _{±0.00}	79.39 _{±0.09}	6.00 _{±0.00}
MEA-D	74.15 _{±0.01}	64.35 _{±0.12}	73.53 _{±0.74}	51.03 _{±3.32}	72.93 _{±0.04}	36.84 _{±0.46}	74.06 _{±0.03}	3.62 _{±0.81}
Blend	81.14 _{±0.02}	99.23 _{±0.03}	80.45 _{±0.06}	87.90 _{±1.12}	80.35 _{±0.02}	6.35 _{±1.85}	80.56 _{±0.45}	3.53 _{±0.91}
WaNet	87.05 _{±0.04}	81.43 _{±2.71}	86.35 _{±0.72}	12.51 _{±1.48}	85.24 _{±0.53}	0.83 _{±0.83}	86.89 _{±0.30}	0.25 _{±0.25}
Composite	85.81 _{±0.70}	92.84 _{±1.05}	85.42 _{±0.76}	74.99 _{±1.02}	84.61 _{±0.00}	0.59 _{±0.59}	86.19 _{±0.25}	5.96 _{±0.85}

Table 9: Sensitivity Analysis of WRK Hyperparameters

WM	ϵ	$\alpha = 0.05$		$\alpha = 1.0$		$\alpha = 1.5$	
		ACC	WSR	ACC	WSR	ACC	WSR
EWE	0.01	91.49 _{±0.15}	48.45 _{±1.64}	91.12 _{±0.16}	30.95 _{±9.83}	91.82 _{±0.08}	90.99 _{±0.15}
	0.03	91.04 _{±0.10}	6.50 _{±1.10}	91.44 _{±0.08}	8.75 _{±1.75}	91.16 _{±0.14}	8.31 _{±0.71}
	0.05	89.14 _{±0.41}	2.03 _{±0.25}	88.19 _{±1.02}	0.86 _{±0.08}	89.51 _{±0.79}	4.02 _{±1.36}
MEA-D	0.01	86.60 _{±0.09}	81.20 _{±1.12}	86.91 _{±0.12}	82.38 _{±2.13}	86.29 _{±0.04}	74.64 _{±2.484}
	0.03	86.44 _{±0.11}	50.92 _{±1.24}	85.02 _{±0.20}	15.20 _{±0.96}	85.46 _{±0.12}	7.64 _{±0.28}
	0.05	79.93 _{±0.84}	24.57 _{±0.21}	80.08 _{±0.76}	16.01 _{±0.00}	80.57 _{±0.48}	8.91 _{±0.83}

Table 10: WSR Performance of CFW Across Datasets

Dataset	Victim Model		Copy Model	
	None	WRK	None	WRK
CIFAR-10	100.00 _{±0.00}	94.72 _{±0.07}	91.20 _{±1.15}	65.60 _{±2.00}
CIFAR-20	100.00 _{±0.00}	94.00 _{±0.07}	82.67 _{±1.70}	56.00 _{±1.15}
Imagenette	100.00 _{±0.00}	93.23 _{±2.36}	82.67 _{±2.26}	61.33 _{±2.37}
DBPedia	100.00 _{±0.00}	92.15 _{±0.45}	93.12 _{±0.06}	73.45 _{±1.13}
Speech Commands	98.32 _{±0.11}	93.33 _{±0.07}	92.35 _{±0.64}	70.12 _{±0.64}

Table 11: WSR_{LC} Performance of Representative Baseline Watermarks

WM	Victim Model		Copy Model	
	None	WRK	None	WRK
EWE	100.00 _{±0.00}	19.89 _{±1.07}	99.65 _{±0.33}	22.34 _{±0.63}
MEA-D	100.00 _{±0.00}	19.90 _{±0.33}	99.53 _{±0.04}	15.52 _{±1.03}
Blend	98.43 _{±0.35}	22.83 _{±0.42}	50.86 _{±0.72}	16.49 _{±0.79}

and drops to between 56.00% and 73.45% after WRK removal.

Table 11 reports WSR_{LC} values for representative baseline watermarks. On victim models, all baselines achieve perfect WSR_{LC} before removal. After WRK attacks, however, WSR_{LC} drops dramatically to between 15.52% and 22.83% on victim models and between 15.52% and 22.34% on copy models. This indicates that baseline watermarks fail to maintain clustering structure under removal attacks.

When compared CFW and watermark baselines, CFW demonstrates superior resilience in terms of WSR_{LC} and WSR. While baseline watermarks suffer severe degradation in WSR_{LC} and WSR after WRK removal, CFW maintains high values that reflect its robust clustering structure.

E.7. Resilience of CFW to Additional Removal Attacks

Table 12 compares CFW with nine popular removal techniques and WRK removal on CIFAR-10 victim models and their MEXMI copies. CLP occasionally causes accuracy degradation exceeding 2%, which occurs when at least one neuron must be pruned. From Table 12, we have the following key observations. First, CFW exhibits strong resilience across all evaluated removal attacks, maintaining WSR_{LC} ≥ 96% on victim models and over 72% on copy models. Second, the intra-class variance remains extremely low even after the attack, providing a strong clustering signal for ownership verification. Specifically, variance values are consistently less than one-third of those in non-watermarked models. These results highlight that CFW resists diverse removal strategies by combining class-level watermarking with clustering-based verification.

Table 12: Resilience of CFW against Other Removal Attacks

Removal Metrics/%	Victim Model			Copy Model (MExMI)		
	ACC	WSR _{LC}	Var($\times 10^{-2}$) \downarrow	ACC	WSR _{LC}	Var($\times 10^{-2}$) \downarrow
Non-Watermark	93.55 ± 0.19	12.00 ± 0.67	18.18 ± 4.25	89.81 ± 0.95	11.33 ± 2.67	19.78 ± 4.75
Non-Removal	93.26 ± 0.12	100.00 ± 0.00	1.68 ± 0.45	89.29 ± 1.06	94.00 ± 1.33	2.74 ± 0.95
NC	92.38 ± 0.25	98.67 ± 1.33	1.66 ± 0.42	89.04 ± 1.12	72.67 ± 2.67	5.15 ± 1.85
I-BAU	91.49 ± 0.30	98.67 ± 1.33	1.77 ± 0.50	89.04 ± 0.98	80.00 ± 2.00	3.20 ± 1.25
BTI-DBF	91.57 ± 0.28	96.67 ± 2.67	1.66 ± 0.48	88.15 ± 1.51	72.67 ± 2.67	5.23 ± 1.95
CLP	87.44 ± 0.75	99.33 ± 0.67	2.00 ± 0.65	87.01 ± 0.98	90.00 ± 2.00	4.20 ± 1.65
Fine pruning	84.20 ± 1.25	100.00 ± 0.00	1.78 ± 0.60	67.33 ± 1.02	96.67 ± 1.33	3.16 ± 1.35
NAD	91.76 ± 0.22	98.00 ± 2.00	1.81 ± 0.55	88.20 ± 0.94	73.33 ± 2.67	4.87 ± 1.75
AT	92.15 ± 0.20	99.33 ± 0.67	1.64 ± 0.40	89.23 ± 1.23	73.33 ± 2.67	4.66 ± 1.65
SEAM	92.35 ± 0.18	100.00 ± 0.00	1.72 ± 0.52	88.84 ± 1.41	80.00 ± 2.00	3.54 ± 1.45
FST	91.21 ± 0.32	96.00 ± 2.00	1.61 ± 0.45	89.02 ± 0.98	78.67 ± 2.67	2.85 ± 1.15
WRK	91.95 ± 0.23	96.67 ± 2.67	2.89 ± 0.95	88.37 ± 1.13	79.33 ± 2.67	4.90 ± 1.85

Arrows represent the trend toward better watermark performance.

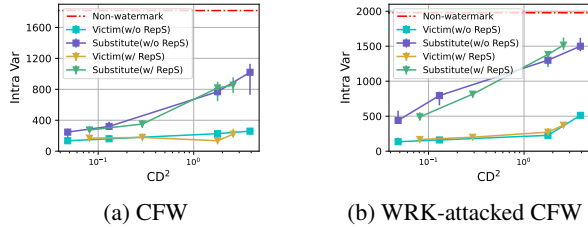


Figure 11: CD^2 versus Intra-class Variance. The vertical lines represent error bars.

E.8. Impact of CD^2 on CFW Stability

This section evaluates the relationship between CD^2 and the clustering stability of CFW, which is measured by intra-class variance. Here, two scenarios are observed: one without an attack and the other with WRK attacks. Each experiment is further divided into two setup conditions: one with RepS and one without. The experiments are conducted on CIFAR-10. Figure 11 visualizes these relationships for each scenario.

First, we observe that CD^2 optimization significantly affects the clustering stability of the copy model. When CD^2 loss (calculated with Equation 6) is below 0.1, both the MEA-post and MEA-removal-post stability of the copy model achieve favorable conditions, with consistently low variance. However, as CD^2 increases, the MEA-post stability (Figure 11a) and removal-post stability (Figure 11b) decline rapidly. These findings indicate that, in terms of representation space clustering, CFW becomes unstable to MEA and removal attacks if CD^2 is not properly optimized. Finally, RepS does not have a clear impact on the stability of watermark tasks.

E.9. Impact of Representation Entanglement (RE) of CFW on MEA Transferability

This section investigates the relationship between the representation entanglement (\mathcal{RE}) and MEA transferability for CFW, evaluated through the copy model’s WSR and WSR_{LC}. Two sets of experiments are conducted: one with CD^2 optimization and one without, where \mathcal{RE} is controlled by the RepS coefficient. The experiments use the CIFAR-10 dataset. The results presented in Figure 12 reveal several key findings. First, when \mathcal{RE} is larger than 0.3, MEA transferability consistently reaches optimal levels. Additionally, even when \mathcal{RE} exceeds 0.8, WSR remains above 50%, pri-

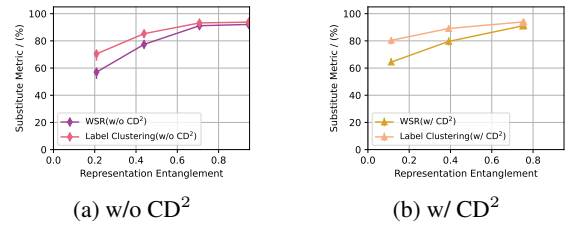


Figure 12: MEA transferability versus the representation entanglement (\mathcal{RE}). The vertical lines represent error bars.

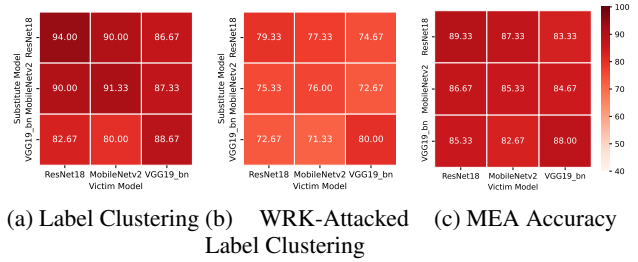


Figure 13: Performance of CFW with different architectures used in model extraction attacks. The horizontal labels are victim models, and the vertical labels are copy models.

marily because CFW is constructed with real-life samples. Lastly, while CD^2 has limited impact on WSR, it significantly enhances WSR_{LC}, achieving over 80% even when $\mathcal{RE} < 0.2$. This improvement is attributed to CD^2 ’s ability to preserve clustering stability during MEA.

E.10. Ablation Study: The Impact of Copy Model’s Architectures on Class-feature Watermarks

In model extraction attacks, the copy model’s architecture used by the adversary usually differs from that of the victim model. Therefore, we study the consistency of CFW across different architectures. Specifically, we cross-test three architectures: ResNet18, MobileNet, and VGG19-bn on CIFAR-10. In this setup, the victim and copy models are assigned different architectures in each combination, and Figure 13 presents CFW’s performance using heatmap grids. The results indicate that CFW’s performance is minimally affected by model architecture, displaying high consistency. This is because the CFW functions as a task and is independent of the underlying architectures.

E.11. Discussions

Piracy Attack. A piracy attack occurs when the adversaries embed their watermarks in a stolen model to evade watermark detection (Liu et al. 2024). This creates ambiguity in ownership verification, as two watermarks exist simultaneously. To prevent such ownership confusion, the simplest countermeasure is to timestamp the watermark model, samples, and verifier through a trusted and accessible platform, such as privately uploading them to an open-source repository. This ensures that even if the adversary performs a piracy attack, they cannot predate the defender’s verified timestamp.

Table 13: CFW Resilience Against False Claim Attacks via Adaptive Watermark Injection

Target Label	Model	ACC/%	Piracy WSR _{LC} /%	CFW WSR _{LC} /%
Same	Victim	90.79 _{±0.08}	62.50 _{±0.18}	100.00 _{±0.00}
	Copy	87.14 _{±0.07}	57.60 _{±0.31}	97.70 _{±0.17}
Cross	Victim	90.69 _{±0.07}	10.00 _{±0.00}	100.00 _{±0.00}
	Copy	86.85 _{±0.41}	32.00 _{±11.85}	92.70 _{±3.86}

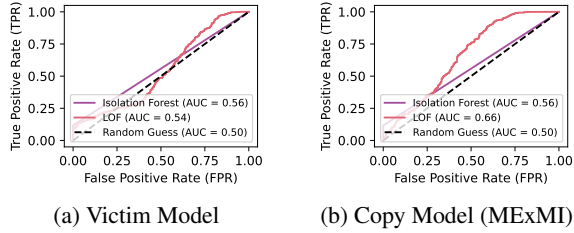


Figure 14: AUC results of abnormal detections on CFW

We experimentally evaluate CFW’s resilience against such piracy attacks under two adaptive injection scenarios. In the same-label scenario, the adversary injects watermarks targeting the same label as CFW. In the cross-label scenario, the adversary targets a different label. Table 13 presents the experimental results on CIFAR-10. The results indicates that even with injected watermarks, CFW maintains strong verification capability. On victim models, CFW achieves perfect WSR_{LC} of 100% under both same-label and cross-label injection attacks. On copy models, CFW maintains WSR_{LC} above 92.70% in both scenarios. In contrast, the injected piracy watermarks achieve significantly lower WSR_{LC} values, ranging from 10.00% to 62.50%. This demonstrates that CFW’s clustering-based verification remains robust even when competing watermarks are present.

Watermark Detection. The section titled *Experiments for Class-feature Watermarks* has yet to discuss the stealthiness property (**Prop.6**). When the stolen model is deployed online, adversaries may filter out potential watermark data and refuse to provide correct query labels to evade watermark verification. To assess CFW’s stealthiness, we evaluate two anomaly detection methods: Local Outlier Factor (LOF) (Breunig et al. 2000) and Isolation Forest (Liu, Ting, and Zhou 2008), applied to the last hidden layer, following EWE (Jia et al. 2021). Since CFW relies on clustering in the representation space, these methods infer watermark queries as high-density points, contrary to their original detection principles. Figure 14 shows AUC results on the CIFAR-10 dataset with 1,200 queries. The highest AUC reached only 0.66, indicating that watermark queries are difficult to distinguish.